BROAD-BAND LIGHT EMISSION FROM ION IMPLANTED SILICON NANOCRYSTALS VIA PLASMONIC AND NON-PLASMONIC EFFECTS FOR OPTOELECTRONICS

Akhilesh K. Singh, B.Sc., M.Sc., M.S.

Dissertation Prepared for the Degree of

DOCTOR OF PHILOSOPHY

UNIVERSITY OF NORTH TEXAS

December 2012

APPROVED:

Arup Neogi, Major Professor
Floyd D. McDaniel, Committee Member
Duncan L. Weathers, Committee Member
Tae-Youl Choi, Committee Member
David Schultz, Chair of the Department of Physics
Mark Wardell, Dean of the Toulouse Graduate School

Singh, Akhilesh K., Broad-Band Light Emission from Ion Implanted Silicon Nanocrystals via Plasmonic and Non-plasmonic Effects for Optoelectronics. Doctor of Philosophy (Physics), December 2012, 69 pp., 32 figures, chapter references.

Broad band light emission ranging from the ultraviolet (UV) to the near infrared (NIR) has been observed from silicon nanoparticles fabricated using low energy (30-45 keV) metal and non-metal ion implantation with a fluence of $5*10^{15}$ ions/cm^2 in crystalline Si(100). It is found from a systematic study of the annealing carried out at certain temperatures that the spectral characteristics remains unchanged except for the enhancement of light emission intensity due to annealing. The annealing results in nucleation of metal nanoclusters in the vicinity of Si nanoparticles which enhances the emission intensity. Structural and optical characterization demonstrate that the emission originates from both highly localized defect bound excitons at the Si/Sio_2 interface, as well as surface and interface traps associated with the increased surface area of the Si nanocrystals. The emission in the UV is due to interband transitions from localized excitonic states at the interface of Si/SiO_2 or from the surface of Si nanocrystals. The radiative efficiency of the UV emission from the Si nanoparticles can be modified by the localized surface plasmon (LSP) interaction induced by the nucleation of silver nanoparticles with controlled annealing of the samples. The UV emission from Si nanoclusters are coupled resonantly to the LSP modes. The non-resonant emission can be enhanced by electrostatic-image charge effects. The emission in the UV (~3.3 eV) region can also be significantly enhanced by electrostatic image charge effects induced by Au nanoparticles. The UV emission from Si nanoclusters, in this case, can be coupled without LSP resonance. The recombination of carriers in Si bound excitons is mediated by transverse optical phonons due to the polarization of the surface bound exciton complex. The low energy side of emission spectrum at low temperature is dominated by 1st

and 2nd order phonon replicas. Broad band emission ranging from the UV to the NIR wavelength range can be obtained from Ag implanted onto a single silicon substrate.

Copyright 2012

By

Akhilesh K Singh

ACKNOWLEDGEMENTS

First of all, I would like to acknowledge the hard work and guidance of my advisor Prof. Arup Neogi and my committee members Prof. Floyd D. McDaniel, Prof. Duncan L. Weathers and Prof. Tae-Youl Choi. It is only their continuous mentoring, encouragement, and trust that I was able to complete this dissertation.

I would like to express my thanks to Prof. Moon Kim and his Post doc Dr. Seong Y. Park from the University of Texas at Dallas for their help in TEM measurements and analysis. I must also thank all my friends and colleagues at UNT for their useful discussions and suggestions.

I would like to express my gratitude to my wife Arpana Singh for her inspiration and continuous support. I must also thank our lovely daughter Ashna. Finally, I would like to dedicate this work to my parents shri Rajendra P. Singh and Chandrika Devi and brothers Gauri S. Singh, Anil Singh and K. P. Singh without their continuous inspiration and support over a long period of time, this work wouldn't have been possible.

TABLE OF CONTENTS

Page

ACKNOWLEDGEMENTS iii

LIST OF FIGURES vi

LIST OF SYMBOLS AND ACRONYMS ix

CHAPTER 1 INTRODUCTION 1

1.1 Introduction 1

1.2 Silicon Nanostructures and Self-Trapped Excitons 2

1.3 Quantum Confinement and Nanostructures 2

1.4 Self-Trapped Excitons (STEs) 3

1.5 Experimental Techniques 3

1.5.1 Photoluminescence (PL) and Photoluminescence Excitation (PLE) 3

1.5.2 Time-Resolved Photoluminescence (TRPL) 5

1.5.3 High Resolution Transmission Microscopy (HRTEM) 5

1.6. References 6

CHAPTER 2 MECHANISM OF LIGHT EMISSION IN LOW ENERGY ION IMPLANTED SILICON 7

2.1 Introduction 7

2.2 Experimental Method 8

2.3 Results 9

2.3.1 Structure and Morphology 9

2.3.2 Spatial Distribution of Luminescence Centers 10

2.3.3 Temperature Dependence and Time Resolved Photoluminescence Spectra 10

2.4 Discussions 15

2.5 Conclusion 16

2.6 References 17

CHAPTER 3 BROAD BAND LIGHT EMISSION FROM Ag -ION IMPLANTED SILICON NANOCRYSTAL 18

3.1 Introduction 18

3.2 Experimental Methods 19

3.3 Results and Discussion 20

3.4 Conclusion 29

3.5 References ... 29

CHAPTER 4 ORIGIN OF ROOM TEMPERATURE BROAD BAND LIGHT EMISSION AND CARRIER DYNAMICS IN Ag ION-IMPLANTED SILICON NANOCRYSTALS ... 31

4.1 Introduction ... 31

4.2 Experimental ... 32

4.3 Results and Discussions ... 33

4.4 Conclusion ... 41

4.5 References ... 42

CHAPTER 5 LOCALIZED SURFACE PLASMON POLARITON ENHANCED RADIATIVE RECOMBINATION IN ION- IMPLANTED SILICON ... 45

5.1 Introduction ... 45

5.2 Results and Discussions ... 47

5.3 Conclusion ... 54

5.4 References ... 54

CHAPTER 6 PHONON REPLICA AND NON PLASMONIC EFFECT IN SILICON NANOPARTICLES IN SILICON MATRIX ... 56

6.1 Introduction ... 56

6.2 Raman Effect ... 56

6.2.1 Classical Theory of Raman Effect ... 57

6.2.2 Raman Spectroscopy (Experimental) ... 59

6.3 Non Plasmonic (Image Charge Effect) ... 60

6.4 References ... 65

CHAPTER 7 SUMMARY AND CONCLUSIONS ... 67

LIST OF FIGURES

Page

Figure 1.1 Photoluminescence arrangement, with He-Cd laser (A), lenses (L1, L2, L3), prism (P), beam block (B), sample (SM) inside cryostat (C), spectrometer (S) and CCD detector (D) 4

Figure 2.1 (a) HRTEM image of silicon ions implanted with 45 keV energy into a silicon substrate (i) Pre-annealed (ii) post-annealed (700 ºC argon) at high magnification; (iii) post-annealed with EDX from different regions. b) Spatial mapping of luminescence centers: fluorescence lifetime imaging microscope (FLIM) image of a 30 µm by 30 µm region of the wafer, observed at 2.97eV of the silicon wafer as implanted with silicon. The color bar also indicates the electron-hole recombination lifetime of the carriers....................11

Figure 2.2 Photoluminescence temperature dependence of blue. All spectra are normalized 12

Figure 2.3 Photoluminescence temperature dependence of UV emissions from the as-implanted silicon wafer. All spectra are normalized. 13

Figure 2.4 Fourier transform infrared spectrum of Si ion implanted silicon substrate. Inset show an enlarged scale for the silicon oxide peak. 14

Figure 2.5 PL spectra showing the high energy peaks present with UV emission (solid line) and blue emission (dotted line). 15

Figure 3.1 High-resolution TEM image showing implantation depth and the region of formation of Si nanoparticles; Pt layers shown in figure is deposited to protect sample surface. 20

Figure 3.2 Images showing distribution of Si NCs. 20

Figure 3.3 Images showing the formation of Ag nanoparticles in the vicinity of Si nanoparticles. 21

Figure 3.4 Histogram showing nanoparticles size distribution....................21

Figure 3.5 Temperature dependent UV PL from Ag implanted Si NCs observed using CW excitation at 325 nm. 23

Figure 3.6 Temperature dependent blue PL from Ag implanted Si NCs observed using CW excitation at 325 nm. 25

Figure 3.7 Temperature dependent green PL from Ag implanted Si NCs observed 26

Figure 3.8 PL and PLE of UV region measured at RT (dashed gray and solid black shows PLE and PL spectra for UV emission respectively). 27

Figure 3.9 Circle, X and square show the PLE spectra taken at detection energy at 2.63 eV, 2.84 eV and 2.98 eV respectively at RT whereas and black line shows the PL spectra at RT of blue region); The inset in fig.3.9 shows (FTIR) spectrum of sample....................28

Figure 4.1(a) HRTEM image showing formation of Si nanocrystals. (b-e) shows the micro PL emission from various sections of the same wafer due to optical excitation with the HeCd laser source. (b) corresponds to the UV emission centered at 3.27 eV nm shown in Fig. 4.3, (c) corresponds to the blue spectral emission as shown in Fig. 4.4, (d) corresopnds to the green spectral emission as shown in Fig. 4. 5, (e) corresponds to red spectral emission as shown in Fig.4. 6. 34

Figure 4.2 shows size distribution of Si NCs formation. 35

Figure 4.3 (a) CW- PL spectrum of UV region at RT with excitation at 325 nm. (b) PL lifetime at 3.25 eV with excitation at 350 nm. 36

Figure 4.4 (a) CW- PL spectra of blue region at RT with excitation at 325 nm. (b) PL life time measured at 2.98 (solid), 2.84 (grey), and 2.63 eV (dashed) at 370 nm excitation. 38

Figure 4.5 (a) CW- PL spectrum of the green region with excitation at either 325 or 442 nm. (b) PL lifetime measured at RT using ps excitation source at 400 nm. 39

Figure 4.6 RT CW- PL emission in the near IR region with excitation at 442 nm. 40

Figure 4.7 PLE spectra measured with the detector in the UV and Blue emission energies to show the presence of electronic states for carrier transitions. 41

Figure 5.1 Localized surface plasmon resonance energy calculated from silver nanoparticles of average size 6.5 nm. The peak surface plasmon resonance energy in this graph is ~3.3 eV. 48

Figure 5.2 High resolution transmission electron microscope with EDX plots showing the presence of Ag nanoparticles in the proximity of Si nanoparticles. The Si nanoparticles are formed by the low energy Ag ion-implantation whereas the nanoscale Ag clusters are formed after annealing the samples at 5000 C. The carbon and copper signal in the EDX plots arise from the sample mount and TEM grid respectively 49

Figure 5.3 Temperature dependent PL from Si implanted Si nanocrystals observed using a CW excitation at 325 nm. PL emission is not observed beyond 160 K..................................50

Figure 5.4 Temperature dependent PL from silver implanted Si nanocrystals observed using a CW excitation at 325 nm. UV PL emission is observed at 300 K in the presence of the Ag nanocrystals...52

Figure 5.5 Shows comparison of time-resolved photoluminescence emission from Si nanoparticles (at 15 K) in the presence of Ag at 3.31 eV. The dotted line represents the PL recombination rate from Si nanoparticle with (dashedline) and without (solid line) the Ag nanoclusters...53

Figure 5.6 Time integrated PL measured at 15 K using femtosecond excitation source at 350 nm. The Purcell enhancement factor (τwo-Ag/τAg) is also shown on the other X-axis and corresponds to the four fold enhancement in the PL emission due to the pulsed laser excitation. 54

Figure 6.1 Energy level diagram for Raman scattering; (a) Stokes Raman scattering (b) anti-Stokes Raman scattering. 57

Figure 6.2 Raman spectra of Si unimplanted and Ag implanted in Si sample. 60

Figure 6.3 A comparison of normalized extinction coefficient (dotted lines) with respect to the room temperature PL emission energy from Si nanocrystals for Ag ion implanted sample. 63

Figure 6.4 A comparison of normalized extinction coefficient (lines) with respect to the room temperature PL emission energy from Si nanocrystals for Au ion implanted sample............64

LIST OF SYMBOLS AND ACRONYMS

1-D: One- dimensional

2-D: Two- dimensional

3-D: Three-dimensional

Ag: Silver

Au: Gold

CW: Continuous wave

EDX: Energy dispersive X-ray spectroscopy

eV: Electron volt ($1.602176565*10^{-19}$ J)

FLIM: Fluorescence lifetime imaging microscopy

FWHM: Full width at half maximum

Ga: Gallium

HeCd: Helium cadmium

HeNe: Helium neon

HRTEM: High resolution transmission electron microscopy

IQE: Internal quantum efficiency

LA: Longitudinal acoustic

LO: Longitudinal optical

LSP: Localized surface plasmon

nm: Nanometer (10^{-9} m)

PL: Photoluminescence

PLE: Photoluminescence excitation

QD: Quantum dot

QW: Quantum well

RT**:** Room temperature

SEM**:** Scanning electron microscopy

Si: Silicon

SP: Surface plasmon

SPP: Surface plasmon polariton

SPR**:** Surface plasmon resonance

STEs: Self-trapped excitons

TA: Transverse acoustic

TEM**:** Transmission electron microscopy

Ti:Sapph: Titanium sapphire

TO: Transverse optical

TRPL: Time resolved photoluminescence

XRD: X-ray diffraction spectroscopy

CHAPTER 1

INTRODUCTION

1.1 Introduction

Silicon has proven as a dominant material since 1950 and will be a key material for the next generation technology. In this dissertation, I present the mechanism of broad band light emission from silicon nanoparticles. This work discusses the mechanisms and origins of broad band light emission, as well as modification and enhancement mechanisms.

The reasons silicon is important for technological uses and a key material for industry is that silicon is both abundant in nature and comparatively inexpensive. Silicon is considered for "siliconizing" photonics, which is one of the key goals of most of the semiconductor industry seeking technological breakthroughs. Once, we can succeed in generation of tunable broad band light emission, and making modulators, optical amplifiers, lasers and wavelength converters to switch a signal's from silicon, the realization of "siliconizing" photonics can be fulfilled which can lead to new era of technology.

The mechanisms of broad band light emission from silicon nanoparticle formed by metal and non- metal ions implanted in silicon wafers will be presented in the first few chapters followed by the enhancement of light emission and carrier dynamics in subsequent chapters.

Silicon wafers were implanted with metal and non-metal ions, such as silver, gold, and silicon etc., for the formation of silicon nanoparticles. Subsequent preparations included annealing, chemical etching, and thin film deposition.

The formation of silicon nanoparticles were confirmed by high resolution transmission microscopy (HRTEM) and X-ray diffraction spectroscopy (XRD), along with other analytical tools such as Raman spectroscopy, Fourier transform infrared spectroscopy (FTIR), and energy dispersive X-ray spectroscopy (EDX). Broad band light emission was

confirmed by photoluminescence (PL). The origin and detail mechanisms were determined by time resolved photoluminescence (TRPL). This work provided further evidence of phonon replica and image charge effects, which can be very important for both device technology and basic research. The detail concerning these phenomena will be presented in last few chapter of this dissertation.

1.2 Silicon Nanostructures and Self-Trapped Excitons

It is well-known that silicon does not emit light from bulk structure [13]. However, Si emits light from different types of nanostructures, which has a wide range of applications in the fields of silicon photonics, optoelectronics, and different silicon-based devices. Therefore, it is very important to understand the concepts of nanostructures and excitons.

1.3 Quantum Confinement and Nanostructures

In general, we study the behavior of material in a three –dimensional system. However, modern solid state physics allows the possibility of studying physics in lower dimensions. This lower dimension solid state system consists of no degrees of freedom in one or two spatial dimensions. These lower dimension systems are called quantum confined systems. As well studied and established in semiconductor materials, the examples of 2-D, 1-D and 0-D are a quantum well, quantum wire and quantum dot. In the case of a quantum well, carriers in the well have no degree of freedom of motion in the direction perpendicular to the plane layer, due to the fact that they must all in the same quantum state [1]. The quantum structure with one spatial degree of freedom (two confined dimensions) is called a quantum wire, whereas the quantum structure with no spatial degree of freedom (confines carriers in all three dimensions) is called a quantum dot. These structures are called quantum confined nanostructures and study of these types structure is called nanoscience. In addition

to these structures, we also study many different types of excitons in the vicinity of these nanostructures such as defect –bound excitons, self-trapped excitons, etc.

1.4 Self-Trapped Excitons (STEs)

In a semiconducting material, electron–hole pairs, bound by a coulomb attraction, are called excitons. Excitons can produce a strong electric field at a lattice site, which may lead to a distortion of the crystal structure. This can eventually lead to trapping of the electrons and holes at different sites so that they cannot recombine. This is called self-trapped excitons.

The self-trapped excitons (STEs) are one of the important radiation-induced defects in silicon. Excitons in silicon self-trap from low temperatures to at least room temperature [2 – 12]. Self-trapping occurs in an otherwise ideal structure when the excited electron and hole spontaneously create a localized distortion in the lattice which lowers their total energy and thus localizes and traps them at the distortion. "Self-trapped excitons" are stabilized because of the widening of the gap induced by the confinement. This effect is not restricted to the case of silicon crystallites but, from general considerations discussed in the following, is likely to be valid for all types of semiconductor crystallites.

1.5 Experimental Techniques

1.5.1 Photoluminescence (PL) and Photoluminescence Excitation (PLE)

PL spectroscopy is a contact less, nondestructive method of probing the electronic structure of materials by using different wavelength of laser depending upon the electronic structure of a sample. PL setup is shown in figure 1.1. Generally, light is directed onto a sample, where it is absorbed and imparts excess energy into the material in a process called photo-excitation. In this process, photo-excitation causes electrons within the material to move into permissible excited states. Upon returning to their equilibrium states, the excess

energy is released through the emission of light. In this case of photo-excitation, this luminescence is called photoluminescence [14]. The energy of the emitted light or PL is related to the difference in energy levels between the two electronic states involved in the transition. The intensity and spectral content of this photoluminescence is a direct measure of various important material properties [15].

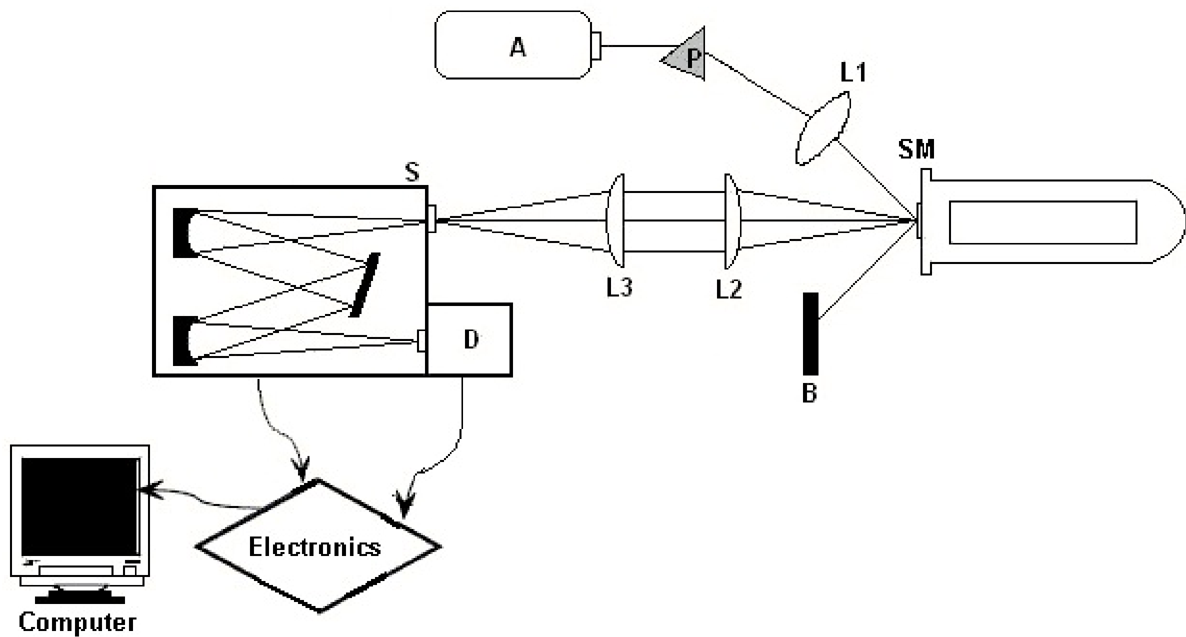

Figure 1.1 Photoluminescence arrangement, with He-Cd laser (A), lenses (L1, L2, L3), prism (P), beam block (B), sample (SM) inside cryostat (C), spectrometer (S) and CCD detector (D).

PL setup consists of the following:

- Laser (He- Cd 325 and 442 nm)
- Optics (convex lens, filters, prism, sample holders)
- Spectrometer (Horiba-Jobin Yvon's 320 Triax)
- CCD (Charge coupled device)
- Cryo-pump
- SpectraMax™ software

The detail is also described [16].

Photoluminescence (PLE)

This is a specific type of photoluminescence and concerns the interaction between electromagnetic radiation and matter. In this spectroscopic measurement, the white light source is used as source of excitation instead of laser light as mentioned in the case of PL. White light is passed through a monochromater to vary the wavelength of excitation which incident on the sample of interest. Peaks in the PLE spectra often represent absorption lines of the material. PLE emission is detected at a fixed wavelength while excitation wavelength is scan (by a monochromator or tunable laser) to obtain emission intensity vs. excitation wavelength. In the case of PL, excitation wavelength is fixed; emission intensity vs. wavelength is obtained by scanning a monochromator of spectrometer as described above.

1.5.2 Time-Resolved Photoluminescence (TRPL)

For the time-resolved PL a mode-locked, Spectra Physics Mai-Tai Ti: Sapphire, laser was used as the excitation source. The wavelength of excitation is varied depends on experiment using doubler and tripler nonlinear crystals. This resulted in pulses of about 80 femtosecond duration with intrinsic repetition rate of 80 MHz. The time-resolved PL was analyzed using a Bruker 250IS spectrograph and detected by a Hamamatsu C4334 Streakscope. The wavelength of excitation for different regions was used different which will be described in experimental part of each section.

1.5.3 High Resolution Transmission Microscopy (HRTEM)

For high resolution transmission electron microscopy (HRTEM), the high-resolution imaging TEM is a JEOL 2100 F which is a 200kV field emission TEM facility available at University of Texas at Dallas has been used.

1.6. References

1. David W. Snoke, Solid state Physics: Essential concepts (Addison- Wesley, 2009).
2. W Hayes, M J Kane, O Salminen, R L Wood and S P Doherty, J. Phys. C **17**, 2943 (1984).
3. M. A. Stevens Kalceff and M. R. Phillips, Phys. Rev. B **52**, 3122 (1995).
4. D. L. Griscom, Proceedings of the Thirty-Third Frequency Control Symposium (Electronic Industries Association, Washington, DC, p. 98 (1979).
5. L.W. Hobbs and M. R. Pascucci, J. Phys. (Paris), Colloq. **41**, C6-237 (1980).
6. S. Guizard, P. Martin, G. Petite, P. D'Oliveira and P. Meynadier, J. Phys. Condens. Matter **8**, 1281 (1996).
7. K. Tanimura, T. Tanaka, and N. Itoh, Phys. Rev. Lett. **51**, 423 (1983).
8. K. Tanimura and L. E. Halliburton, Phys. Rev. B **34**, 2933 (1986).
9. C. Itoh, K. Tanimura, and N. Itoh, J. Phys. C **21**, 4693 (1988).
10. W. Joosen, S. Guizard, P. Martin1, G. Petite, P. Agostini1, A. Dos Santos, G. Grillon, D. Hulin, A. Migus, and A. Antonetti, Appl. Phys. Lett. **61**, 2260 (1992).
11. P. N. Saeta and B. I. Greene, Phys. Rev. Lett. **70**, 3588 (1993).
12. Sohrab Ismail-Beigi and Steven G. Louie, Phys. Rev. Lett. **95**, 156401(2005).
13. X. L. Wu, F.S. Xue, Appl. Phys. Lett. 84, 2808 (2004).
14. J. D. Cutnell, K. W. Johnson, Physics, Fifth Edition, John Wiley & Sons Publications, NY, 2001.
15. R. A. Riebau, Photoluminescence Spectroscopy of Strained InGaAs/GaAs Structures, thesis dissertation, University of Maryland at Baltimore County, 2002.
16. P. R. Vemuri, Surface plasmon based nanophotonics optical emitters, master thesis, University of North Texas, 2005.

CHAPTER 2

MECHANISM OF LIGHT EMISSION IN LOW ENERGY ION IMPLANTED SILICON[+]

2.1 Introduction

Silicon, an indirect bandgap semiconductor, is known to have over one hundred luminescence centers [1]. Although various luminescence centers in silicon are reported, none of these are deemed suitable for practical application due to a lack of basic understanding of the nature of these emissions. Efficient light emission from Si may play an important role in many technological innovations including monolithically integrated optoelectronic circuits and inexpensive LEDs. Silicon is both inexpensive and well integrated in industry for its electrical properties, making it an attractive material for industrialization of optoelectronic devices.

Light emission from silicon was previously observed from dangling bonds, quantum confinement, and porous silicon (PS) [2,3,4,5]. Ion beam implantation, followed by other treatments such as annealing, is currently a prevalent technique for formation of light emitting Silicon systems [6]. The origin of light emission in ion-implanted Si based semiconductors has been primarily attributed to nanoparticles that are formed after annealing of the samples following the implantation process [2, 6, 7]. These emissions are predominantly due to indirect or quasi-direct transitions in the near-infrared wavelength region and have recently been observed in the UV wavelength regime [2]. These conclusions are based on observation of nanoparticle formation using transmission electron microscopy and resulting far-field luminescence from the implanted sample. However, to the best of our knowledge, no investigations were done on luminescence from ion beam implanted samples based on the microscopy of the light emission, which had traces of the nucleation of

[+] This entire chapter is reproduced from [K.G. Gryczynski, A. K. Singh, A. Neogi, Seong Y .Park, M. Kim, "Mechanism of light emission in low energy ion implanted silicon", J. Lumin. **131**, 2621-2624 1 (2011).], with permission from Elsevier.

nanoparticle formation in the substrate.

These nanoparticles in the ion-implanted samples are reported to typically emit via intraband transitions [8] and surface traps at the interfaces of Si NCs and the surrounding dielectric [6]. These transitions are dominated by Auger recombination process and are generally inefficient at room temperatures. There are also recent unsubstantiated reports of UV emission due to the direct transition from the ion-implanted Silicon nanoparticles [2]. In this study we present the spatially map of the light emission from ion-implanted Silicon using high resolution optical microscopy in the UV-visible region. By investigating the origin of the emissions at various energies, we find the contribution from defect bound excitons that result in strong light emission.

Irradiation with energetic particles, including ions, is known to create various luminescent defect centers within the lattice of silicon [1, 9, 10]. Luminescent defect states generally have excellent photo stability, high quantum yields, and may be formed within the smallest amount of crystalline matter or any macroscopic size sample [11].

2.2 Experimental Method

Phosphorous doped, n-type Si(100) wafers were obtained from University Wafer, Boston MA. The wafers were implanted by Core Systems, Sunnyvale CA, with Si^+ ions with an energy of 45 keV, ion current of 22 μA, 7° tilt, and an ion fluence of $5x10^{15}$ ions cm^{-2} into an area of 133.4 cm^2 of the wafer.

The internal structure of the implanted wafers was observed with an analytical high resolution TEM (AHRTEM). Annealing was performed in a chemical vapor deposition (CVD) chamber with an Argon atmosphere. Far field PL from the wafers was mapped using a Fluorescence Lifetime Imaging Microscope (FLIM) PicoQuant MicroTime 200 with a 370 nm semiconductor laser diode. Temperature dependent PL was taken with a Horiba-Jobin

Yvon's TRIAX 320 spectrometer and the excitation was provided by an Omnichrome 56 series continuous wave HeCd laser . Time resolved photoluminescence was measured with a Hamamatsu synchroscan streak camera with a resolution of 30ps. The excitation source for lifetime measurements was a Spectra Physics Mai-Tai Ti: Sapphire mode-locked laser. The 700 nm laser output was doubled with a nonlinear BBO (β-Barium Borate) crystal to 350nm.

2.3 Results

2.3.1 Structure and Morphology

HRTRM micrographs reveal that the ion implantation initially results in the formation of an amorphous layer with its depth depending on the penetration distance or the momentum of the implanted ions. However, the crystalline nature can be recovered by annealing the samples at 700º C. PL from the wafer was observed after just the implantation and after implantation and annealing of the wafer. Since TEM shows no nanoparticles for all samples (fig 2.1a) the luminescence observed from Silicon in this experiment is not associated to the formation of nanoparticles as reported in various previous reports [2, 6-8]. Instead, the luminescence centers (LCs) are believed to be lattice defect sites formed at the interface of the amorphous and crystalline layers within the wafer and show no signs of photo bleaching. The emission is stable and the wafer may be stored in air for months and sonicated in organic solvents without any discernable changes to the emissions. Figure 2.1a shows the sample structure after implantation for both pre annealed and after annealing at 700 ºC. The depth of the implanted region is found to be ~ 115 nm using TEM as shown in figure 2.1a-i, which is in agreement with SRIM simulations [12]. Defect and interfacial states are created and concentrated near the crystalline and amorphous silicon boundary where some polymorphous silicon is present. However, after annealing the sample at 700 ºC in Argon, the thickness of the implanted layer changed. A flat interface between the SiO_2 layer and crystalline Si is

observed as shown in figure 2.1a-iii. The amorphous layer is no longer present. It is observed that defect areas consisting of dislocations are formed at a depth of 118 nm from the surface. The resulting wafers were found to luminescence from the ultraviolet to the visible wavelength region. Annealing resulted in a higher concentration of LCs, but no new emission energies and no emission energy shifts were observed due to annealing.

The emission from the annealed samples is significantly brighter due to formation of the crystalline layer and the localization of defects. Thus light emission from silicon was achieved using only silicon as the implantation source and target.

2.3.2 Spatial Distribution of Luminescence Centers

In order to spatially map the optical emission from the Si implanted sample, luminescence microscopy with sub-micron resolution was performed. Fig. 2.1b presents a typical 30μm by 30μm fluorescence imaging microscopy map of the sample surface at room temperature for the un-annealed sample. Luminescence was observed at a single emission energy, 2.97eV, the false color scale represents the average lifetime of the observed emission. Black regions in the image, corresponding to parts of the sample surface, have very weak or low light emission, and thus they have no measureable PL lifetimes. Far field measurements confirm this scattered distribution of the emission centers. The distribution of the LCs throughout the silicon wafer arises from the self-assembly of LCs which are governed by the concentration of impurities and defect centers along the crystalline silicon lattice.

2.3.3 Temperature Dependence and Time Resolved Photoluminescence Spectra

Photoluminescence (PL) spectra were measured at temperatures ranging from 15K to 300K, fig. 2.2-2.3. The blue luminescence (fig. 2.2) originates from known silicon oxide defect states, and along with the EDX (fig 2.1a-iii) and FTIR (fig 2.4) data, is proof of the presence of oxygen within the wafer.

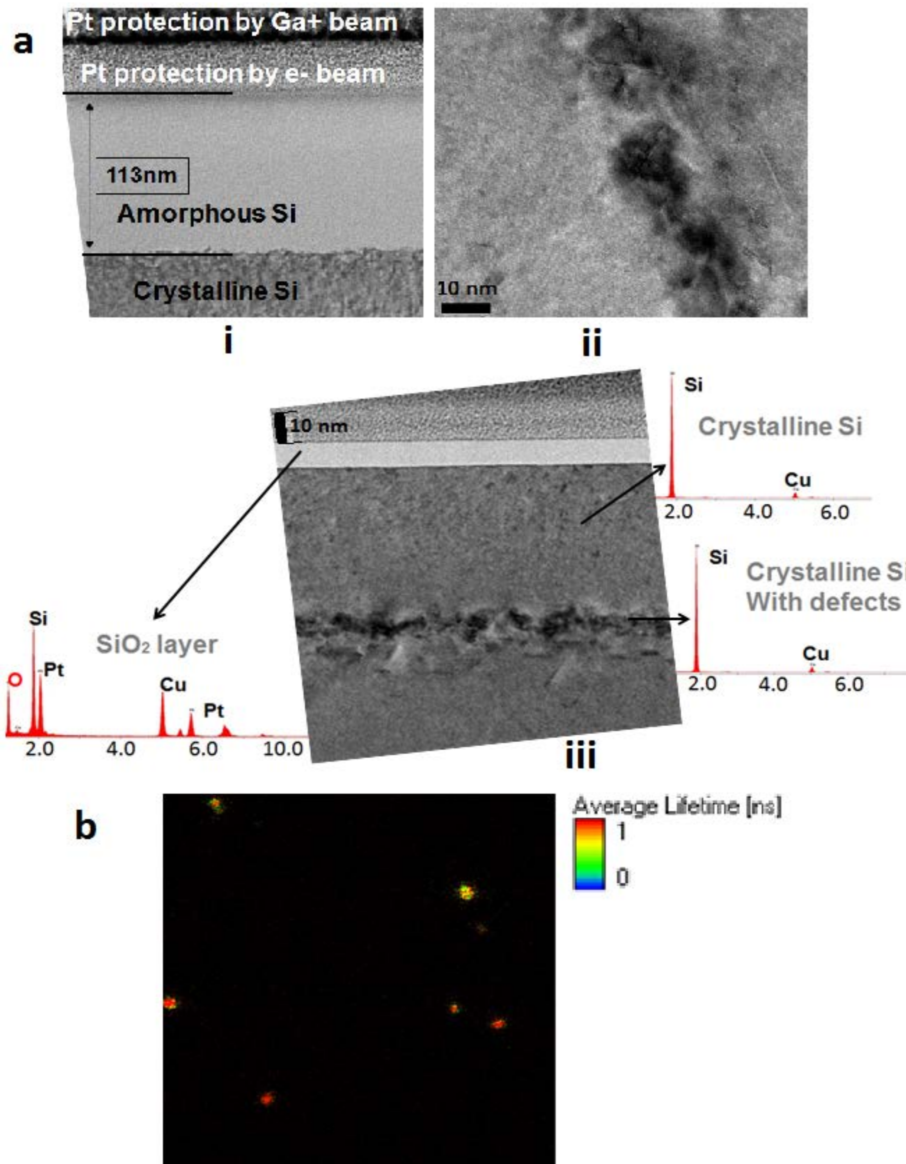

Figure 2.1 (a) HRTEM image of silicon ions implanted with 45 keV energy into a silicon substrate (i) Pre-annealed (ii) post-annealed (700 ºC argon) at high magnification; (iii) post-annealed with EDX from different regions. b) Spatial mapping of luminescence centers: fluorescence lifetime imaging microscope (FLIM) image of a 30 µm by 30 µm region of the wafer, observed at 2.97eV of the silicon wafer as implanted with silicon. The color bar also indicates the electron-hole recombination lifetime of the carriers.

Oxygen is a common impurity in silicon wafers, and it is observed in the present system. The presence of the infrared absorption band approximately at 1250 cm^{-1} which is due to the SiO_3 group has been reported to be the origin of luminescence in Si oxide nanostructures [17]. The oxidation of the annealed samples makes it possible for the strong emission according to DFT calculations [3]. Silicon oxides in the sample are most likely formed around crystalline and

poly-crystalline damaged sites in low concentrations, making their presence difficult to confirm by HRTEM-EDX. The luminescence peaks at 2.98 eV and 2.84eV are likely to be from excess of si defects centers in si nanostructures [13]. The PL lifetime as observed from the FLIM measurement exhibits recombination rates in the nanosecond limit, these lifetime measurements (fig. 2.1b) are further evidence that these peaks are previously observed defect states. The peak at 2.64eV was previously observed in $Si0_2$ wafers implanted with Si and attributed to $Si0_2$ defect states [6]. Peak intensities, FWHMs, and relative peak intensities for these peaks are not noticeably affected due to temperature variation, as expected for these defects. However, different LCs may have different relative peak intensities of these prominent blue emissions.

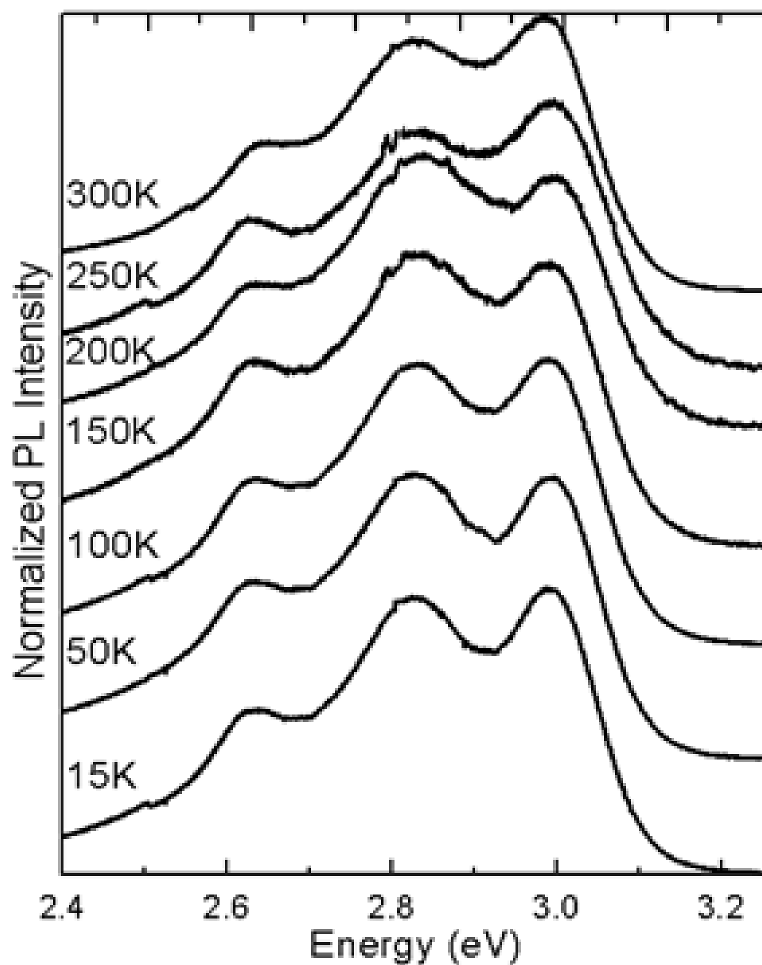

Figure 2.2 Photoluminescence temperature dependence of blue. All spectra are normalized.

Fig. 2.3 shows the temperature dependent PL for a typical UV emitting region. Similar to the LCs emitting in the blue wavelength region, these higher energy emission are distributed throughout the wafer. In unannealed samples, the emission intensity decreases with temperature. No luminescence is observed beyond 200K from the as-implanted samples, indicating a low concentration of these LCs.

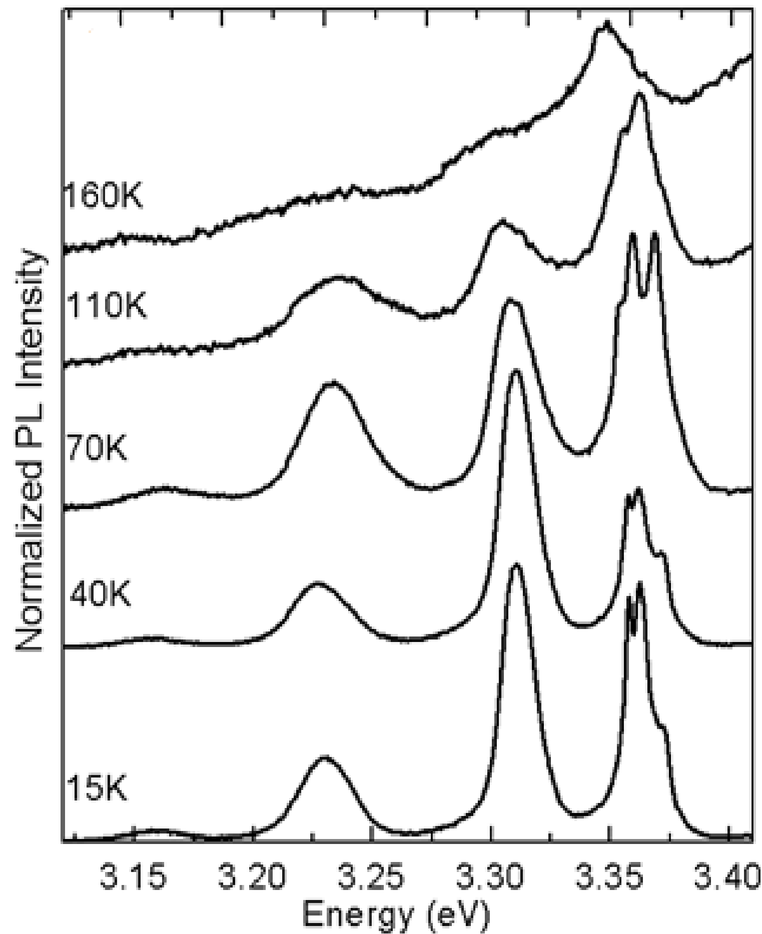

Figure 2.3 Photoluminescence temperature dependence of UV emissions from the as-implanted silicon wafer. All spectra are normalized.

However, these emissions for the annealed sample are visible at RT indicating enhancement. These emissions broaden and combine into a single discernably broad peak as temperature is increased (fig 2.3). The temperature dependence of these peaks is identical in the un-annealed and annealed samples showing that their origin is similar. At low temperatures, the peak emission at 3.3 eV is attributed to excitons bound to the lattice defect states. This emission

exhibits large temperature dependence and its FWHM plotted versus temperature fits a Bose Einstein distribution.

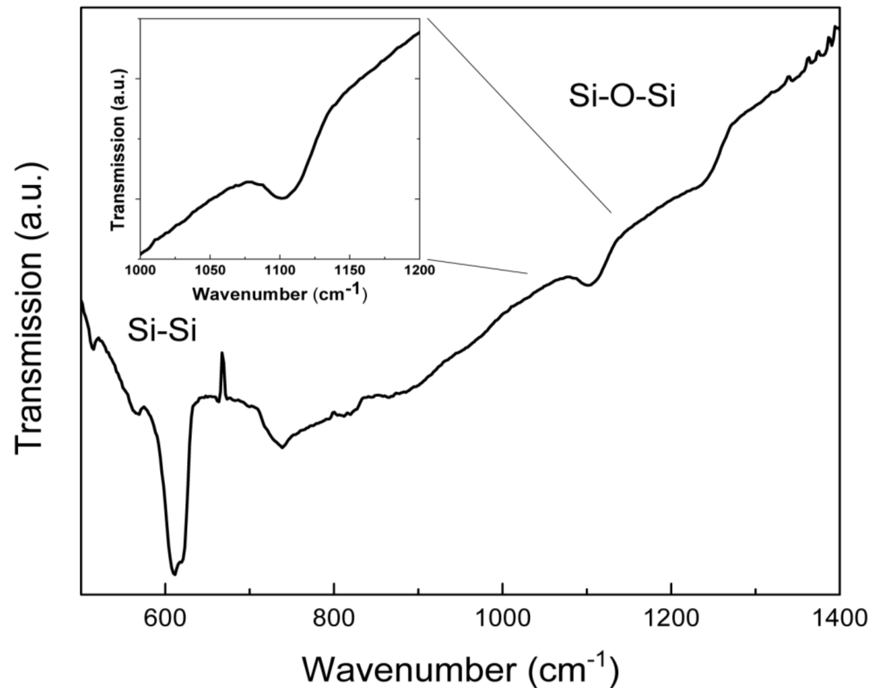

Figure 2.4 Fourier transform infrared spectrum of Si ion implanted silicon substrate. Inset show an enlarged scale for the silicon oxide peak.

At 15 K, it has a sub nanosecond lifetime (fig 5.5) which indicates strong confinement and distinguishes this emissions from luminescence originating from non-bridging oxygen hole centers (NBOHC) which are often reported for porous silicon [14, 15]. Previous reports of sub-nanosecond lifetimes in Si were observations of quasi-direct bandgap transitions [16]. The weak emission peaks with energies ~60 meV and ~120 meV lower than the confinement peak are phonon replicas of the exitons confined in the lattice defects.

The group of peaks at 2.356 eV is always visible with the UV emission. Figure 2.5 shows two spectra, one with a prominent UV peak and blue peaks absent, and one with blue peak dominate and the UV peaks barely above noise level, both have a strong peak at 3.356 eV. Both these spectra come from different sites on the same un-annealed wafer. This group of high energy emission peaks is comprised of at least four narrower peaks, which are often resolvable. These peaks are not observed at RT and exhibit strong temperature dependence.

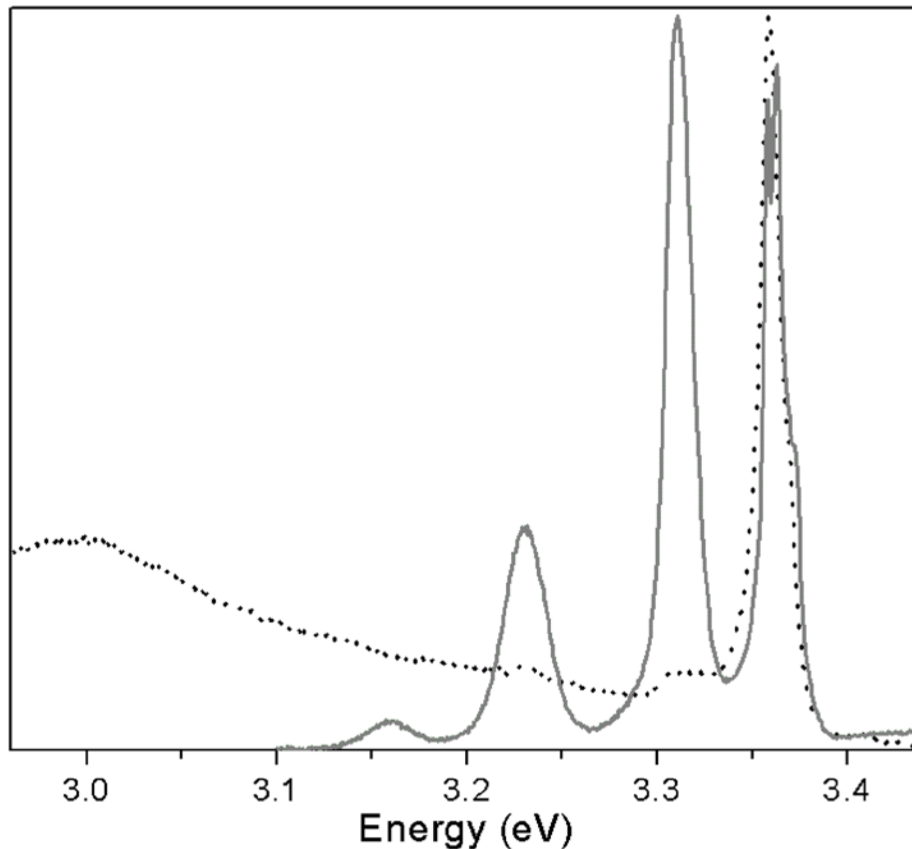

Figure 2.5 PL spectra showing the high energy peaks present with UV emission (solid line) and blue emission (dotted line).

Their relative intensities and FWHMs change at different rates relative to temperature (fig 2.5). The individual peaks from this group have FWHMs as low as ~1meV. The lifetimes of these peaks are ~0.2 ns (fig 5.5), which is another indication that these peaks most likely originate from silicon oxide surface interfaces with silicon [17].

2.4 Discussions

At most luminescence centers either the blue peaks, or the UV emission centers are observable. However, at some sites both sets of peaks are visible, and either set may dominate the emission. This behavior is attributed to the self-assembly of oxides by the silicon implantation used to fabricate the sample. Various emission centers may be formed in any location within the wafer, independently of any other structures in the vicinity. An arbitrary excitation cross section may have any combination of luminescence color centers

within it, with no emission from certain regions. The intensity of a given peak is dictated by the concentration of the structure responsible for the emission and its distance from the surface. Modeling of Urbach absorption and free carrier absorption for the laser excitation used (325nm) in amorphous silicon indicates that the intensity of laser light at 115nm is 83 % of the original intensity.

$$I(z) = I_0 * e^{-\alpha_0 \frac{E-E_G}{E_G} * z}$$

Where z is the distance traveled by the light, α_0 the absorption constant for silicon ($1*10^4 cm^{-1}$), E the energy of the laser (3.815eV), and E_G the bandgap energy of amorphous silicon (1.7eV). 83% of the excitation pulse reaching the crystalline regions of the wafer is the minimum efficiency, which can be improved by implanting the ions not as deep, but by varying the energy of implantation. It is also possible to reduce the thickness layer of the Silicon above the LC or defect centers in the implanted silicon wafer through chemical etching to reduce the emission from the LC's which has a higher inter-bandgap compared to bandgap of the surrounding Silicon cap layer.

2.5 Conclusion

Light emission from silicon was achieved through the formation of crystal defect sites and silicon oxides in a silicon matrix by ion implantation. The produced luminescence centers are stable and the wafer may be stored in atmosphere. The ability to produce multiple wavelength emission from a single wafer through the same process may be useful for producing inexpensive white light emitters. Further investigation into the formation process is necessary to control the location and distribution of emitting regions throughout the wafer. Post processing such as annealing and etching may be used to enhance the emission and will be investigated in the near future.

2.6 References

1. G. Davies, PHYSICS REPORTS (Review Section of Physics Letters) 176. Nos. 3 & 4, 83-188 (1989).

2. G. Sahu, H.P. Lenka, D. P. Mahapatra, B. Rout, F.D. McDaniel, J. Phys.: Condensed. Matter 22, 072203 (2010).

3. T. Kim, N. Park, K. Kim, G. Sung, Y. Ok , T. Seong and C. Choi, Appl. Phys. Lett. **85**, 5355 (2004).

4. N. Park, C. Choi, T. Seong, and S. Park, Phys. Rev. Lett. **86**, 1355(2001).

5. D. Zhang, R.M. Kolbas, P.D. Milewski, D. J. Lichtenwalner, A. I. Kingon, J.M. Zavada, Appl. Phys. Lett. **65**, 356 (1998).

6. H. Z. Song, X. M. Bao, Phys. Rev. B **55**, 6988 (1997).

7. L.J. Mitchell, F. Naab, O.W. Holland, J.L. Duggan, F.D. McDaniel, J. of Non-Crystalline Solids **352**, 2562 (2006).

8. I. Sychugov, R. Juhasz, J. Valenta, J. Linnros, Phys. Rev. Lett. **94**, 087405 (2005).

9. A. V. Mudryi, A. I. Patuk, I. A. Shakin, F. P. Korshunov, V. A. Zuev, Materials Chemistry and Physics **45**, 185 (1996) .

10. S. Godefroo, M. Hayne1, M. Jivanescu, A. Stesmans, M. Zacharias, O. I. Lebedev, G. Van Tendeloo, V. V. Moshchalkov,. Nature **3**, 174 (2008).

11. Y. Chang, H. Lee, K. Chen, C. Chang, D.Tsai, C. Fu, T. Lim, Y. Tzeng, C. Fang, C. C. Han, H. Chang, W. Fann, Nature Nanotechnology **3**, 284 (2008).

12. J.F. Ziegler, SRIM: the Stopping and Range of Ions in Matter (computer program), http://www.srim.org.

13. S. L. Johnson, P. A. Heimann, A.M. Lindenberg, H.O. Jeschke, M. E. Garcia, Z. Chang, R.W. Lee, J. J. Rehr, R.W. Falcone, Phys. Rev. Lett. **91**, 15 (2003).

14. Y. Zhanga, Z. Yangb, D. Niua, E. Niea, X. Baia, Z. Jiaoa, Y. Jina, M. Gongb, X. Sun, Applied Surface Science **256**, 3325 (2010).

15. Y. Zhanga, Z. Yangb, D. Liua, E. Niea, X. Baia, Z. Lia, H. Songa, Y. Zhoua, W. Lib, M. Gongb, X. Sun, Journal of Luminescence **130**, 1005 (2010).

16. M. Sykora1, L. Mangolini, R. D. Schaller, U. Kortshagen, D. Jurbergs, V. I. Klimov, Phys. Rev. Lett. **100**, 067401 (2008).

17. R. Ferre, I. Martín, M. Vetter, M. Garín, R. Alcubilla, Appl. Phys. Lett. **86**, 201906 (2005).

CHAPTER 3

BROAD BAND LIGHT EMISSION FROM Ag -ION IMPLANTED SILICON NANOCRYSTAL*

3.1 Introduction

Quantum confined (QC) Si nanostructures are commonly used to obtain optical emissions from Si [1-2], which does not emit light in bulk form. Luminescence from Si has many applications in optoelectronics including light emitting diodes [3]. Silicon photonics based on Si nanoparticles has received renewed interest due to its possible application in monolithically integrated optoelectronic circuits to realize lower threshold emitters, detectors, or modulators with higher packing densities. Light emission, due to electron-hole recombination in Si nanoparticles, has been reported due to quasi-direct transitions in QC Si nanostructures [1], annealing induced recombination processes via stable oxygen–related defect center [4], and surface state induced recombination processes [5].

One of the most common Si based nanocrystals synthesis techniques for very large-scale integration (VLSI) compatibility involves the use of ion beam implantation [6, 7, 8]. The implantation dose and energy can be used to control the size of the nanoparticles and thereby the wavelength of light emission. The density and depth of Si nanocrystals (NCs) in the solid matrix can also be controlled by these parameters. The size of Si NCs normally achievable using ion-beam implantation techniques yields emission in the near- infrared wavelength regime (700-900 nm) [8].

The origin of emission has been attributed to QC Si nanostructures in which emission is due to bandgap recombination [9]. The emission is also attributed to surface traps at the interface of Si NCs and the surrounding dielectric [10].

* This entire chapter is reproduced from [A. K. Singh, K. G. Gryczynski, S. Y. Park, M. Kim, and A. Neogi, "Broad band light emission from Ag- ion implanted silicon nanocrystals," Solid State Commun. **151**, 1405–1409 (2011)], with permission from Elsevier.

The emission from the Si NCs can be tuned from the UV to the near-infrared range using magnetron scattering techniques [1]. Even if the origin of light emission from Si is from highly localized defects, a consensus has been reached that both highly localized defects at the Si/SiO_2 interface [10-12] and the quantum confinement (QC) play important roles [11-13, 14]. To confirm more closely the origin of the emissions, i.e. whether it is from QC or highly localized defect states, an estimation using effective mass theory has been carried out, which shows that the emissions don't come from QC effect. In this dissertation, we present the modification of light emission using ion beam techniques for the fabrication of Si nanoparticles, which results in emission from the UV to the green regime from a single wafer. Current approaches to the synthesis of Si nanoparticles use high-energy ion implantation in the MeV range, which can result in non-radiative defect centers in the crystal lattice. In this study, we use a low-energy ion beam (32 keV) for the nucleation of Si nanoparticles followed by annealing to reduce the surface and defect –induced non-radiative processes. We also briefly present the enhancement of UV light emission due to resonant plasmonic interactions from Si nanoparticles.

3.2 Experimental Methods

The Si nanoparticles were fabricated at room temperature (RT) using commercial ion beam implantation of phosphorous doped, n-type Si(100) (resistivity 1–22 Ohm-cm) with Ag ions. The Si wafers were implanted with 32 keV Ag ions of fluence 5×10^{15} ions cm^{-2}. The implantations were carried out at room temperature (RT), at beam currents ~ 200 nA. This was done using a low energy implantation facility, available at the commercial vendor's facility at California [7]. The samples were annealed in air and Nitrogen at 500 °C for 1 h. Continuous wave (CW) - PL measurements were performed with a Horiba – Jobin Yvon's

Triax 320 spectrometer. The 325 nm Helium-Cadmium (He-Cd) laser was used as the excitation source.

3.3. Results and Discussion

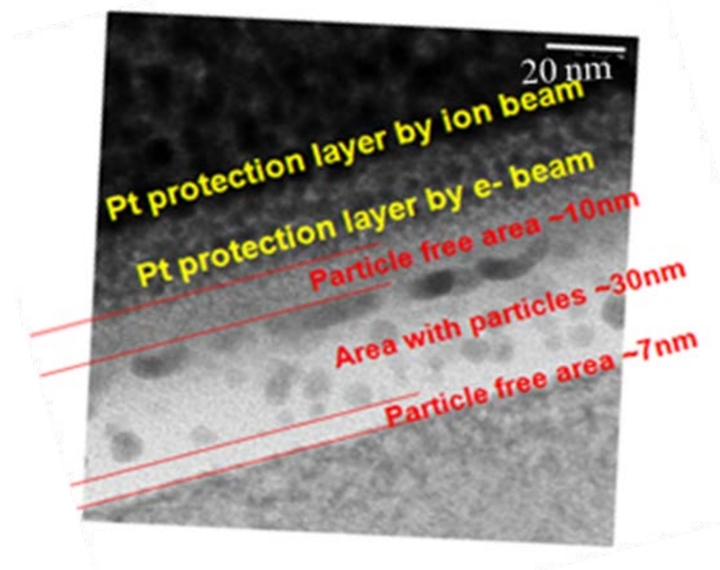

Figure 3.1 High-resolution TEM image showing implantation depth and the region of formation of Si nanoparticles; Pt layers shown in figure is deposited to protect sample surface.

Si nanoparticles are formed by ion implantation using a low-energy ion beam. Formation of nanoparticles is confirmed by HRTEM. The platinum (Pt) layers have been deposited to protect the surface while preparing the sample for HRTEM. There were no Pt layers on the Si samples before the ion implantation.

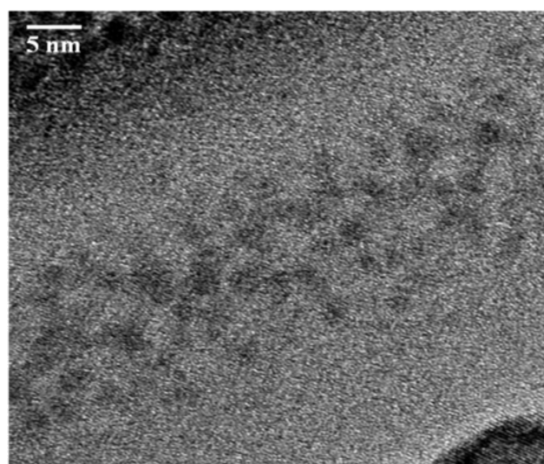

Figure 3.2 Images showing distribution of Si NCs.

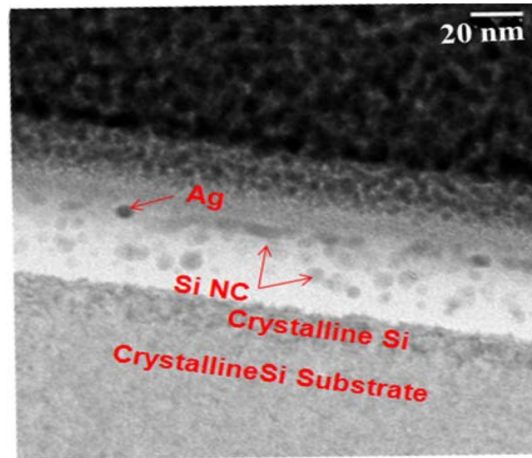

Figure 3.3 Images showing the formation of Ag nanoparticles in the vicinity of Si nanoparticles.

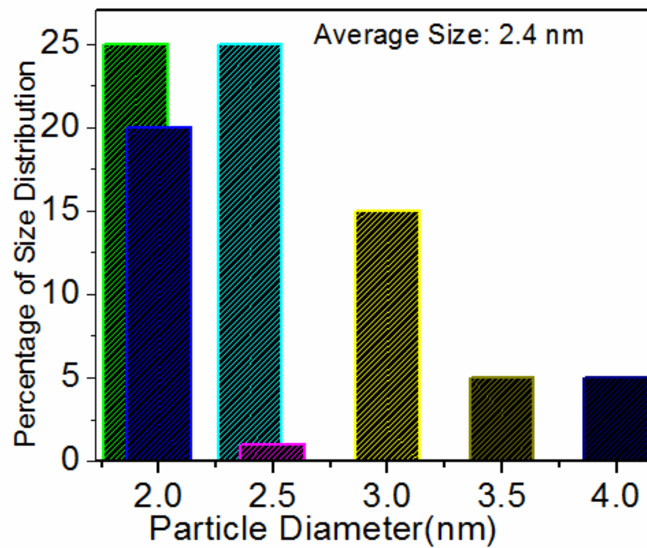

Figure 3.4 Histogram showing nanoparticles size distribution.

HRTEM image in figure 3.1-3.3 shows the formation of Si nanoparticles, which emit broad-band light emission from the UV to the green. It is observed from figure 3.1 that the particles are distributed at the top of the middle region. The Stopping and Range of Ions in Matter (SRIM) simulation estimates reveals that the nanoparticles nucleates around the maximum energy of the ions penetrating the Si(100) lattice. The different size of nanoparticles as shown in histogram (figure 3.4) based on TEM micrographs ranges from 1.9 nm to 4 nm can be easily seen from HRTEM image (figure 3.3) which we believe to be the

source of broad-band light emission. The samples were annealed in air and Nitrogen at 500 °C for 1 h for surface passivation and modification of the size of the nanoparticles formed in the matrix. The green emission is observed only after annealing in an oxygen rich environment and does not occur in the as-implanted samples. Annealing under nitrogen or any other inert gas such as Argon does not change the green emission significantly. There is no significant difference between annealed in air and Nitrogen. Ag nanoclusters were not observed before annealing but appear after annealing as shown in figure 3.2. Therefore, we believe that annealing increases the nucleation of Ag nanoclusters in the sample. The formation of Ag nanoclusters plays a vital role in the presence of localized surface plasmon polariton (LSPP) modes which enhances the efficiency of light emission significantly. The presence of these LSPP is further supported by the Mie scattering modeling [7]. The peak LSPP energies for the size of the silver nanoparticles that are nucleated in the Si matrix are estimated to be ranging from 2.4-3.3 eV. So, the emission from Si emitters in the UV region can be enhanced and RT emission can be observed due to exciton-plasmon coupling induced by the Ag-induced localized surface plasmons polaritons at the surface of the nanoparticles.

The theory of quantum confined (QC) effects has been developed for nanoscale semiconductor on the assumption of Mott-Wannier- type excitons [15, 16]. The energy of excitons in semiconductors rises with decreasing size of nanoparticles as

$$E\,(D) = 2\hbar^2\pi^2/m^*_{e\text{-}h}D^2$$

where effective mass of the exciton is taken as $m^*_{e\text{-}h} = m^*_e\, m^*_h/m^*_e + m^*_h$, E (D) is measured from the minimum excitonic energy to bulk materials, D is the diameter of nanoparticles and m^*_e and m^*_h are effective mass of electron and hole masses [29]. In the present ion-beam implanted Si NCs, for the average diameter of 2.4 nm as shown in figure 3.1-3.3 and summarized in figure 3.4, is expected to have a quantum confined state with energy at E(D)= 1.25 eV. Similarly, for the diameters of 1.9, 2.0, 2.5, 3.0, 3.5 and 4.0 nm, the expected

confinement energies are in the near-infrared wavelength range ranging from 1.30, 1.24, 1.20, 1.18, 1.17, and 1.16 eV respectively. In these estimates, m^*_{e-h} =18.22 * 10^{-31} kg has been considered for the weak QC [17].

The experimentally observed PL peaks emission are ~ at 3.27, 2.98, 2.84, 2.63 and 2.4 eV, which are much larger than the calculated theoretical values of the QC as mentioned above. The high energy emission in the visible and UV wavelength range, as shown in figure 3-3, indicates that these emissions are not due to purely quantum confinement.

Figure 3.5 shows the temperature dependence PL emission in the UV region measured using HeCd laser source of excitation wavelength of 325 nm. The PL spectrum peak centered at 3.27 eV was observed at RT. A possible mechanism for the origin of UV emission is likely to arise from the highly localized defects at the interface of Si/SiO_2.

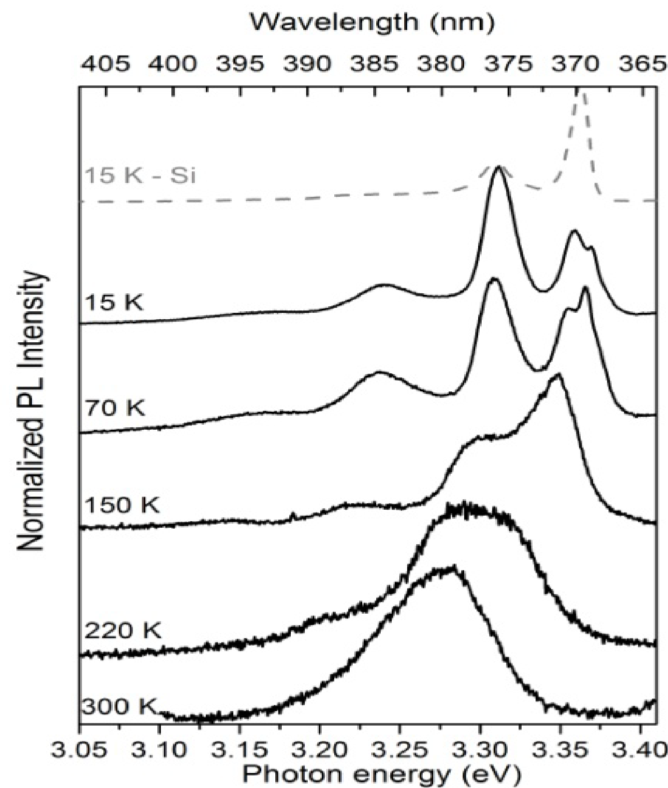

Figure 3.5 Temperature dependent UV PL from Ag implanted Si NCs observed using CW excitation at 325 nm.

The temperature dependent behavior of PL from NCs shows that the dominant lines

centered on 3.3 eV and around 3.37 eV have different origin. The emission at 3.30 eV originates from confined defect bound-excitons, whereas the emission at 3.37 eV is presumably from surface states. The confined defect-bound excitonic transition is confirmed by Bosonic behavior of the broadening factor. Due to the strong confinement of the bound excitons in the Si NCs, negligible peak energy shifts are observed for the transition at 3.3 eV before the peaks merge at higher temperature. The emission from surface states exhibits a relatively larger red- shift with temperature.

As observed in case of magnetron sputtered Si QDs [1], the surface emission can be very strong and in the present case dominates the 3.3 eV bound-exciton transition below 55 K. However, due to non-radiative recombination at the interface layer, the emissions from the surface states are quenched at RT. In the case of localized emissions, the temperature dependence is weaker and the radiative emissions are less influenced. However, in quasi-2D structures like interface or quantum well structures, the emissions at lower temperatures are dominated by the radiative process, which results in more efficient emission compared to emission from NCs at ~ 3.3 eV.

Figure 3.6 shows the temperature dependence PL emission in blue region. The PL spectra observed in this region peak centered at 2.98, 2.84, and 2.63 eV. The origin of the PL emission for peaks centered at 2.98 and 2.84 eV is likely to be from excess Si defect centers in Si nanostructures [14]. The two peaks have an energy interval of about 0.14 eV which is very close to the earlier report of energy interval of about 0.13 eV [14]. The PL emission peak centered at 2.63 eV is related to O_2 vacancies in SiO_3 [18]. RT emission is also observed in this region without any modification in the luminescence energy. There is no temperature dependent emission energy shift as observed in the case of the emissions in the UV wavelength regime. The Fourier Transform Infrared (FTIR) spectrum in inset of fig. 3.9 shows Si-O-Si vibration band at ~ 1100 cm^{-1}, which is a strong indication of excess Si defects

in Si nanostructures. There is no size dependence of the nanoparticles resulting in the blue-emission. In this case, as in the case of UV emission, effective mass theory does not permit the emission in the higher energy regime. The blue emission is observed in the as-implanted samples without annealing.

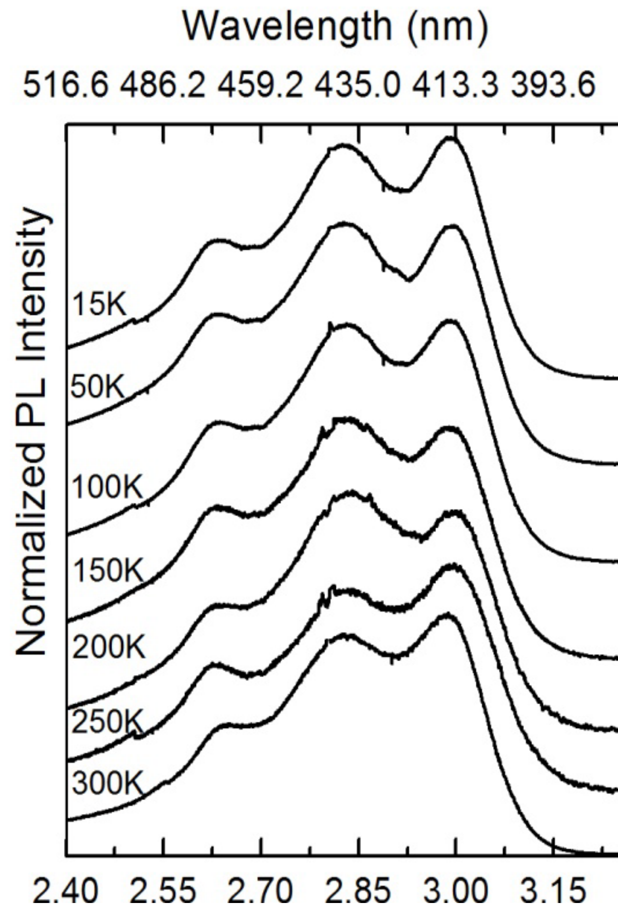

Figure 3.6 Temperature dependent blue PL from Ag implanted Si NCs observed using CW excitation at 325 nm.

Figure 3.7 shows the temperature dependence PL emissions in the green region. The PL emissions at RT in this region has an emission peak ~ at 2.4 eV. The emission is due to the surface related localized states of self-trapped excitons, rather than the excitonic or free-carrier based quantum confined states. The self-trapped excitons are considered to take into account the localization of electrons and holes at the Si/SiO_2 interface. The mechanism for emission in the green region is similar to the reports by Pan et al. where they have described the origin of the emissions from surface–trapped excitons [19].

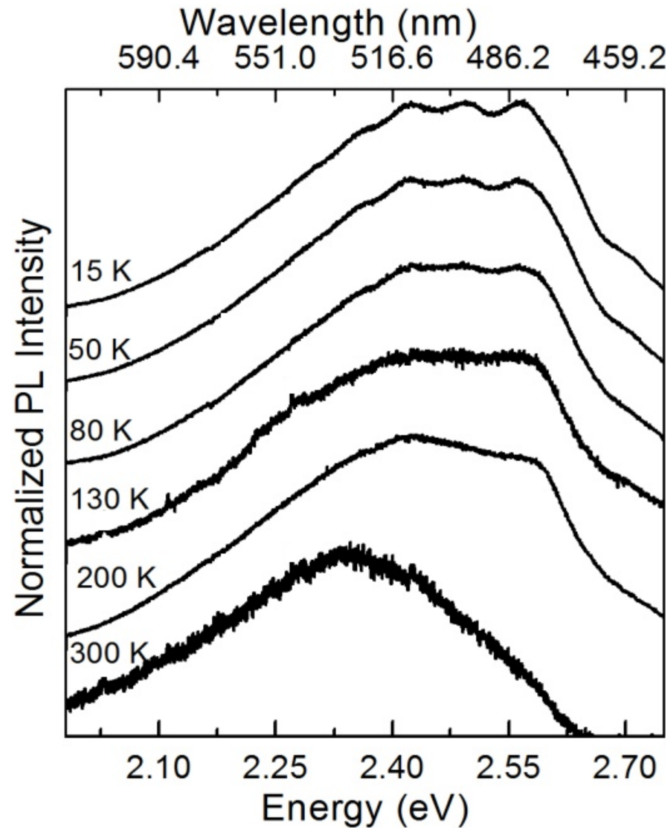

Figure 3.7 Temperature dependent green PL from Ag implanted Si NCs observed**.**

The origin of the emissions is believed to be from highly localized defects at the Si/SiO_2 or from QC states; both play important roles as described elsewhere [20]. The green emission is observed only after annealing in an oxygen rich environment and does not occur in the as-implanted samples. Annealing under nitrogen or any other inert gas such as Argon does not change the green emissions significantly. However, the emission intensity in the green region is significantly enhanced due to the annealing process. It is possible that the nanoparticles migrate towards the surface of the Si substrate during annealing, which reduces the re-absorption of the PL emissions in the green wavelength regime within the Si matrix. Moreover, the nucleation of Ag nanoparticles in the matrix also occurs during annealing, which also increases the probability of LSPP induced enhancement in the photoluminescence signal.

Figure 3.8-3.9 show the absorption states associated with the light emission in the UV

and visible wavelength regimes as measured from PL Excitation measurements. The presence of higher energy states at 4.14 eV is observed, which is likely to influence the emissions at 3.27 eV (Fig. 3.8).

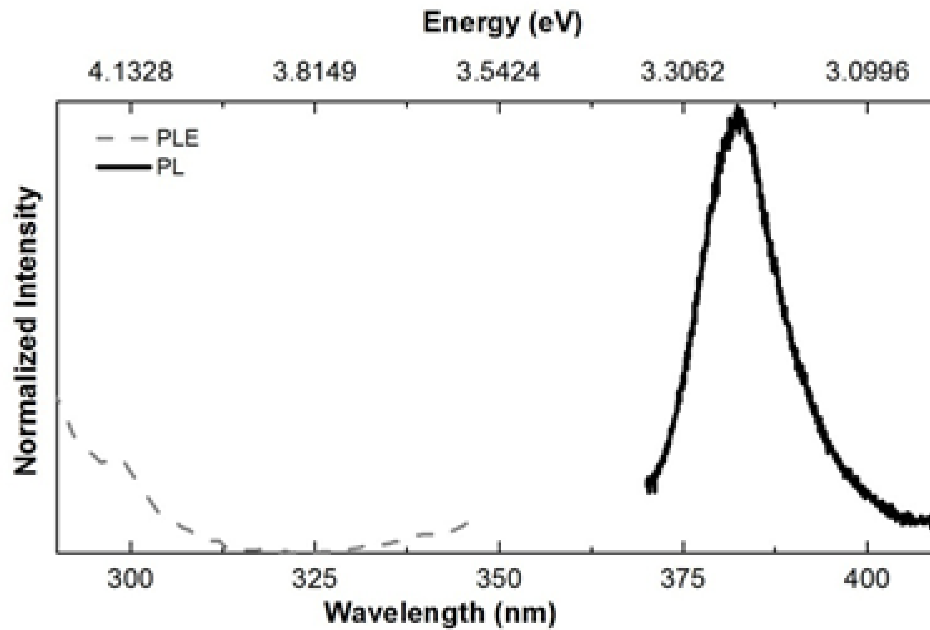

Figure 3.8 PL and PLE of UV region measured at RT (dashed gray and solid black shows PLE and PL spectra for UV emission respectively).

An optical excitation above 4.14 eV is not necessary to observe the UV emission since a HeCd laser at 3.82 eV can o associated with the light emission in UV and visible wavelength regime as measured from PL Excitation measurements. The presence of higher energy states at 4.14 eV is observed which is likely to influence the emission at 3.37 eV (Fig. 3.8). An optical excitation above 4.14 eV is not necessary to observe the UV emission as a HeCd laser at 3.82 eV can result in the emission at 3.27 eV. However, the presence of other absorption states close to 3.27 eV could not be measured due to the strong emission at that state. The presence of a state closer to the UV emission at ~ 3.3 eV is observed from the PLE measurements shown in figure 3.9. In Fig.3.9, the PLE is measured with the detectors at the various emission peaks in the blue wavelength regime (at 2.98 eV, 2.84 eV, and 2.63 eV). It is observed that along with the higher energy state at 4.14 eV shown in Fig. 3.8, the presence of another higher energy state at 3.28eV also exists. The presence of the 3.28 eV peak is

independent of the detection energy. The blue emission can be observed only with an excitation above 3.28 eV. However, the green emission can be observed with a laser excitation below 3.28 eV .

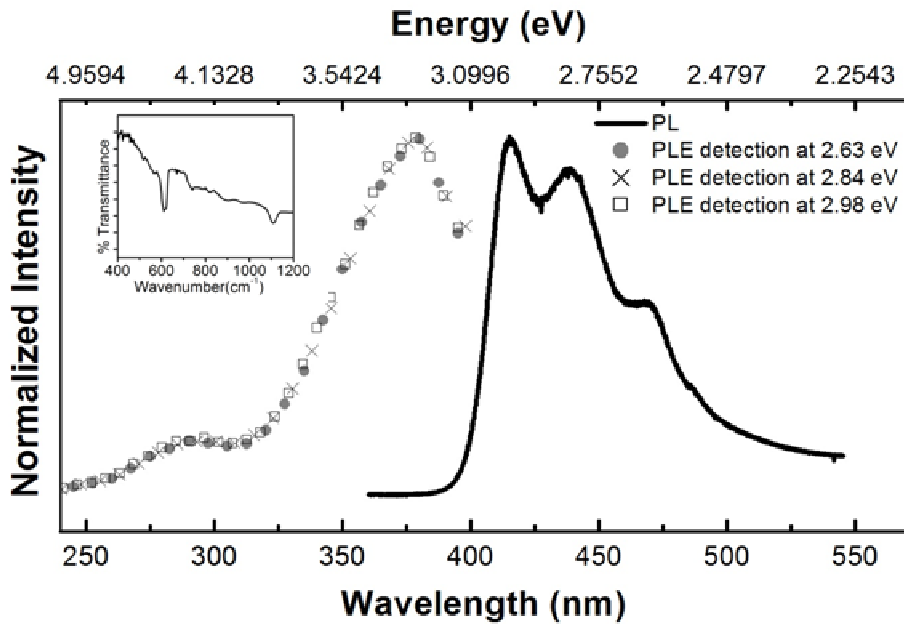

Figure 3.9 Circle, X and square show the PLE spectra taken at detection energy at 2.63 eV, 2.84 eV and 2.98 eV respectively at RT whereas and black line shows the PL spectra at RT of blue region); The inset in fig.3.9 shows (FTIR) spectrum of sample.

It is observed from figure 3.8 that the UV emission at 3.27 eV has its origin from the absorption above energy states exceeding 4.45 eV. This is uncharacteristic of emission from quantum confined structures of emissions from a state closer to the UV emission at ~ 3.3 eV is observed from the PLE measurements shown in figure 3.9. In Fig.3.9, the PLE is measured with the detectors at the various emission peaks in the blue wavelength regime (at 2.98 eV, 2.84 eV, and 2.63 eV). It is observed that along with the higher energy state emission at 4.14 eV shown in Fig. 3.8, the presence of another higher energy state emission at 3.28 eV also exists. The presence of the 3.28 eV peak is independent of the detection energy. The blue emission can be observed only with an excitation above 3.28 eV. However, the green emission can be observed with a laser excitation below 3.28 eV. It is observed from figure

3.8 that the UV emission at 3.27 eV has its origin from the absorption above energy states exceeding 4.45 eV. This is uncharacteristic of emission from quantum confined structures.

3.4 Conclusion

In conclusion, we have observed broad-band tunable light emissions from the UV to the green in Silver ion implanted Silicon substrates. The behavior of PL emissions in UV region suggests the origin of the emissions is from highly localized defects at the Si/SiO_2 interface. Luminescence in the blue and green regions is also observed and the origin is also possibly from defects at the Si/SiO_2 interface. CW photoluminescence, combined with PLE and effective mass theory, suggests that the origin of broad band emission is from surface trapped excitons. Further detailed quantitative study of the synthesis process is necessary for the generation of nucleation centers for controllable surface trapped excitons or quantum confined emissions. The realization of efficient Silicon based broadband emitters can fulfill the requirement of optoelectronic devices for integrated circuits

3.5 References

1. X. L. Wu, F.S. Xue, Appl. Phys. Lett. **84,** 2808 (2004).

2. T. Y. Kim, N.-M. Park, K.-H. Kim, G.Y. Sung, Y.-W. Ok, T.-Y. Seong, C.-J. Choi, Appl. Phys. Lett. **85,** 5355 (2004).

3. N.-M. Park, C.-J. Choi, T.-Y. Seong, and S.J. Park, Phys. Rev.Lett. **86,** 1355 (2001).

4. B.T. Sullivan, D. J. Lockwood, H.J. Labbe, Z.-H Lu, Appl.Phys. Lett. **69,** 3149 (1996).

5. M. Ruckschloss, B. Landkammer, S. Verpe, Appl. Phys. Lett. **63,** 1474 (1993).

6. A. Arbouet, M. Carrada, F. Demangeot, V. Paillard, G. BenAssayag, C. Bonafos, A. Claverie, S. Schamm, C. Dumas, *J.* Grisolia, M.A.F. Van den Boogaart, *J.* Brugger and L. Doeswijk, J. Lumin. **121,** 340 (2006).

7. A.K. Singh, K.G. Gryczynski, F. D. McDaniel, Seong Y. Park, M. Kim and A. Neogi, Appl. Phys. Express **3,** 102201 (2010).

8. L.J. Mitchell, O.W. Holland, A. Neogi, J. Li. and F.D. McDaniel, J. Non-Crystalline Solids **352,** 2408 (2006).

9. Sychugov, R. Juhasz, Jan Valenta, and J. Linnors, Phys. Rev. Lett. **94,** 087405 (2005).

10. Zhang, R. M. Kolbas, P.D. Milewski, A. I. Kinngon, and J. M. Zavada, Appl. Phys. Lett. **65,** 2684 (1998).

11. Delerue, G. Allan, and M. Lanno, Phys. Rev. B **48,** 11024 (1993).

12. B. Delley and E.E. Steigmeir, Phys. Rev. B **47,** 1397 (1993).

13. S. Ogut, J. R. Chelikowsky and S.G. Louie, Phys. Rev. Lett. **79,** 1770 (1997).

14. X.L. Wu, S.J. Xiong, G.G. Siu, G.S. Huang, Y.F. Mei, Z.Y. Zhang, S.S. Deng, and C. Tan, Phys. Rev. Lett**. 91,**157402**,** (2003).

15. Al. L. Efros and A. L. Efros , Fiz Tekh. Poluprovdn 16, 1209 (1982); Sov. Phys. Semicond. **16**, 772 (1982).

16. L.E. Brus, J. Chem. Phys. **79**, 5566 (1983).

17. Y. D. Glinka, N.H. Tolk, Phys. Rev. B **64,** 085421 (2001).

18. L. Tsybeskov, Ju. V. Vandyshev, and P.M. Fauchet, Phys. Rev. B **49,** 7821 (1994).

19. X.-W. Pan, M.-M Shi, D.-X Zheng, N.L. Liu, G. Wu, M. Wang, H.-Z. Chen, Materials Chemistry and Physics **117,** 517 (2009).

20. S. Godefroo , M. Hayne, M. Jivanescu, A. Stesmans, M. Zacharias, O.I. Lebdev, G. van tendeloo and V.V. Moshchalkov, nature nanotechnology **3,** 174 (2008).

CHAPTER 4

ORIGIN OF ROOM TEMPERATURE BROAD BAND LIGHT EMISSION AND CARRIER DYNAMICS IN Ag ION-IMPLANTED SILICON NANOCRYSTALS*

4.1 Introduction

The indirect bandgap of silicon reduces the radiative recombination to be used as a light emitter. However, the modification of silicon by forming silicon nanocrystals, quantum dots, or porous silicon in the microscopic scale can result in light emission from silicon, though it has not yet been possible to fabricate light emitting devices from such systems. Since the discovery of room- temperature (RT) visible photoluminescence (PL) from porous Si in 1990[1, 2], light-emitting Si from nanostructures has become very interesting because of its huge potential in optoelectronic devices for integrated circuits [3, 4]. There have been reports about red and near infra-red (NIR) light-emitting Si nanostructures; however, the reports on ultraviolet to green region emission requires various synthesis techniques varying from chemical synthesis, etching of porous Si, Si in SiO_2 matrix, etc. There does not exist a single technique to generate broad band emission. UV emitting Si nanocrystals (NC) can be prepared by plasma synthesis [5], and chemical vapor deposition [6]; however, ion beam implantation in SiC or SiN [7, 8, 9 and 26] has been used for the nucleation of Si quantum dots that can have a wide range of light emission. Even though, the origin of light emission from Si is controversial, a consensus has been reached that highly localized defects at the Si/SiO_2 interface [10-12] and the quantum confinement (QC) of excitons both play important roles [13-15].

In this work, we investigate the origin of broadband light emission (UV-red) from Si NCs formed by silver ion beam implantation in crystalline Si substrate using Time-Resolved

* This entire chapter is reproduced from [A. K. Singh, K. G. Gryczynski, and A. Neogi, "Origin of room temperature broadband light emission and carrier dynamics in Ag ion-implanted Silicon nanocrystals," Opt. Mat. Express. 2, 501–508 (2012)], with permission from Optical Society of America.

PL (TRPL) spectroscopy. The ambiguity in the origin of light emission can be resolved by studying the decay rates, which are conventionally in the ms to micro-second range due to the indirect or quasi-direct nature of the transitions in Si light emitters. Current approaches of the synthesis of Si NCs use high-energy ion implantation in the MeV range that can result in nonradiative defect centers in the crystal lattice without any broadband emission. In this study, we utilize a low-energy ion beam (32 keV) and controlled annealing for the nucleation of Si NCs to reduce the surface and defect –induced non- radiative processes.

4.2 Experimental

The Si NCs were fabricated at RT by ion beam implantation of Ag. The substrates used in this work were p doped n-type Si(100) with a resistivity of 1-10 Ohm-cm. Silver ions were implanted into the Si(100) substrate at an energy of 32 keV and with a fluence of $5*10^{15}$ ions/cm^2 at beam currents of 250 nA. The implanted samples were thermally annealed in atmospheric O_2 at 500^0C, 600^0C and 700^0C for an hour. The annealing was performed below the Ag-Si eutectic temperature (835°C). The effect of oxidation during the annealing process was investigated by using an inert gas such as Argon. It is observed from a systematic study of the annealing carried out at these temperatures that the characteristics of the PL emission energy in the UV and the blue region remains unchanged. However, a significant enhancement of light is observed due to the annealing. The emission in the green wavelength region is observed only after annealing in an oxygen rich environment and does not occur in as-implanted samples. Annealing without any oxygen under inert conditions such as nitrogen or Argon does not change the UV and blue emissions significantly and has a very slight influence on the intensity of the green emission. The annealing of the ion implanted wafer results in the formation of silver nanocrystals at depths of up to 40 nm from the surface of the Si substrate. However, for the UV laser with excitation wavelength at 3.81

eV (CW laser) or 3.4 eV (pulsed laser), the penetration depth of the light in the ion-implanted amorphised Si layer is shallow and the subsequent PL observed is within 10 nm -20 nm from the surface. However, the penetration depth for the 2.8 eV excitation (442 nm) is relatively larger (~ 500 nm) in the ion-implanted silicon substrate and has a higher efficiency for the green or red emission. Broad-band efficient RT emission ranging from the UV to the NIR/red was observed from various sections of the single wafer of silicon substrate.

Continuous wave (CW) - PL measurements were carried out using a Helium-Cadmium (HeCd) laser with excitation at 3.81 eV (325 nm) and 2.80 eV (442 nm). The UV and blue emission is observed using the 325 nm excitation, whereas the green and red emission is observed using the 442 nm excitation. The photoluminescence lifetime was measured using a Ti: Sapphire 80 MHz, femtosecond (fs) with an excitation wavelength at 3.4 eV (360 nm), with an average power 100 mW and a Hamamatsu Streak camera for detection. The PL lifetime for the emission in the blue wavelength was measured using a picoQuant system with a 15 picosecond diode laser with an excitation energy at 3.30 eV (375 nm), whereas the TRPL of the green emission was measured using a doubled Ti:Sapphire laser at 400 nm. Various bandpass filters depending on the emission wavelength were used to separate the excitation sources.

4.3 Results and Discussions

High resolution transmission electron microscopy (HRTEM) image in Fig.4.1(a) shows formation of Si NCs in crystalline silicon formed by the ion implantation and annealing processes. NCs of different sizes (1.5 - 10 nm) can be clearly seen from HRTEM image in Fig. 4.1(a), which directly or indirectly play a role for the different colors of efficient broadband RT light emission from the single wafer. All the emissions ranging from the UV to the red has been observed from the Ag ions implanted into the identical Si wafer.

The annealing process also nucleates the formation of Ag nanoclusters in the sample and brings it close to the Si NCs as well as towards the surface. Ag NCs were not observed before the annealing process. The micro-PL emission at various wavelengths (energy) is shown in the Figs. 4.1(b-e). Room temperature (RT) emission can be observed over the entire UV-Visible range. The optical properties have been analyzed using TRPL measurements.

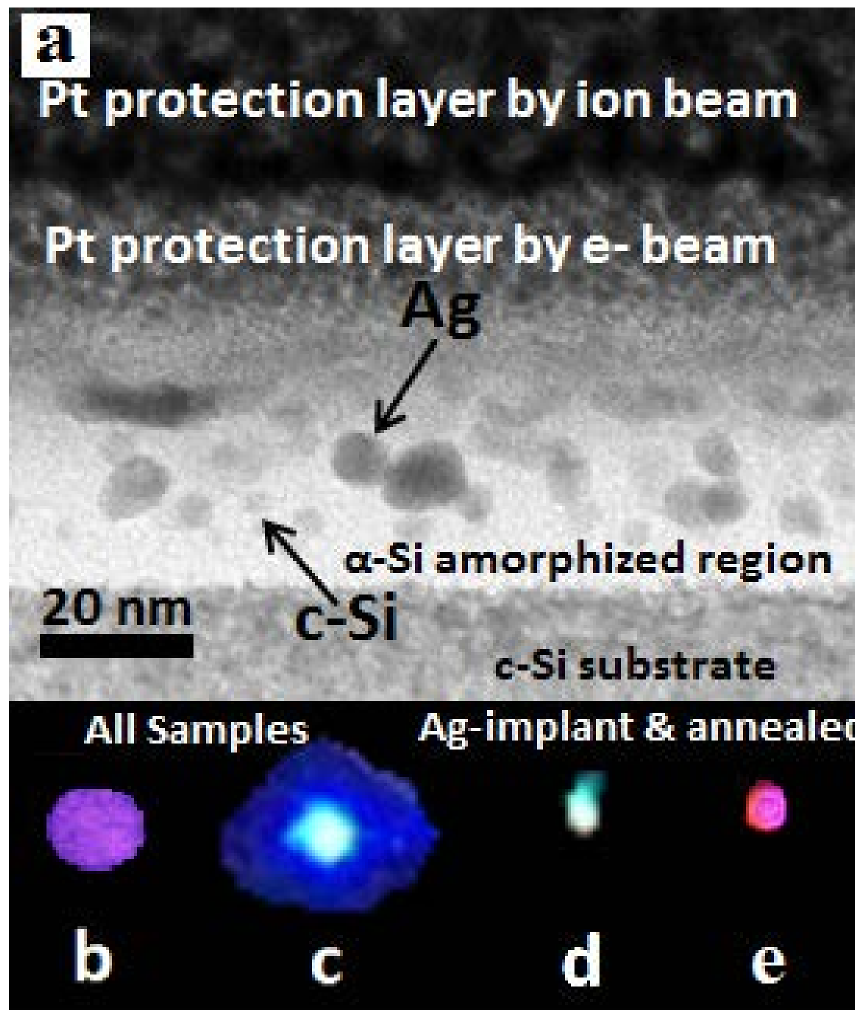

Figure 4.1 (a) HRTEM image showing formation of Si nanocrystals. (b-e) shows the micro PL emission from various sections of the same wafer due to optical excitation with the HeCd laser source. (b) corresponds to the UV emission centered at 3.27 eV nm shown in Fig. 4.3, (c) corresponds to the blue spectral emission as shown in Fig. 4.4, (d) corresopnds to the green spectral emission as shown in Fig. 4. 5, (e) corresponds to red spectral emission as shown in Fig.4. 6.

In the present ion-beam implanted Si NCs, the mean diameter of Si nanoparticle is nearly 2.4 nm as shown in Fig. 4.2. The detail explanation is elsewhere. [17, 18]. The

distributions of size of nanoparticles don't agree with effective mass theory. Thus, emissions ranging from the UV to the red as shown in Fig. (4.3, 4.4, 4.5) indicate that these emissions are not due to quantum confinement effect which will be further strengthened by TRPL analysis. The internal quantum efficiency is measured using the temperature dependent PL spectroscopy by considering that at 15 K the photoluminescence process is dominated by the radiative recombination process with no loss due to non-radiative recombination processes.

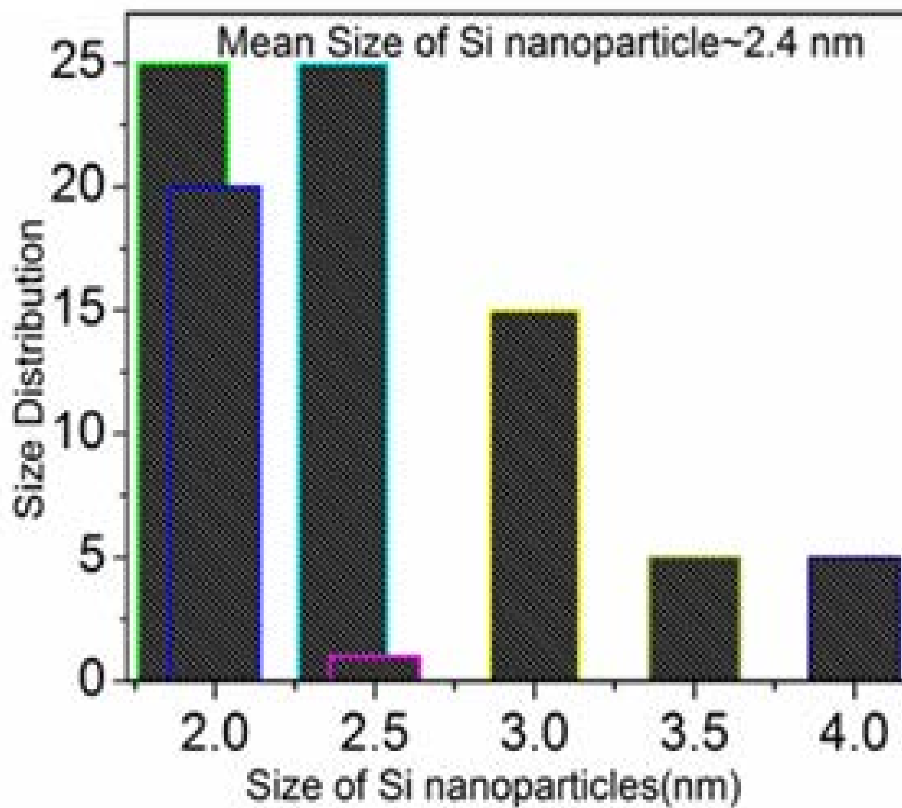

Figure 4.2 shows size distribution of Si NCs formation.

Figure 4.3(a) shows the PL emission from Si NCs which emits at 3.27 eV at RT with a linewidth of ~80 meV. HRTEM micrographs show that the average diameters of the Ag nanoclusters ~6.5 nm. Any UV emissions ranging from 364-384 nm can be resonantly coupled to Ag NCs formed by ion implantation [18]. This wavelength range is suitable for emission from interface states between the Si and its oxide namely the $–SiO_3$ group, which bonds to the Si structural surface and results in a strong 370 nm PL [20]. Similar broadband

UV emission has been reported in silica nano-rings coated with ultra-thin Ag films [27]. However, the emission from these annealed Silica nano-rings in the presence of Ag were limited to the emission at higher energy > 2.9 eV. In our Ag-implanted Si nanocrystal system, the origin of emission in the UV region is from highly localized defects at the interface of Si/SiO_2. The emission from highly localized defects at the interface of Si/SiO_2 plays equally important roles as quantum confined (QC) emission [10-12, 21].

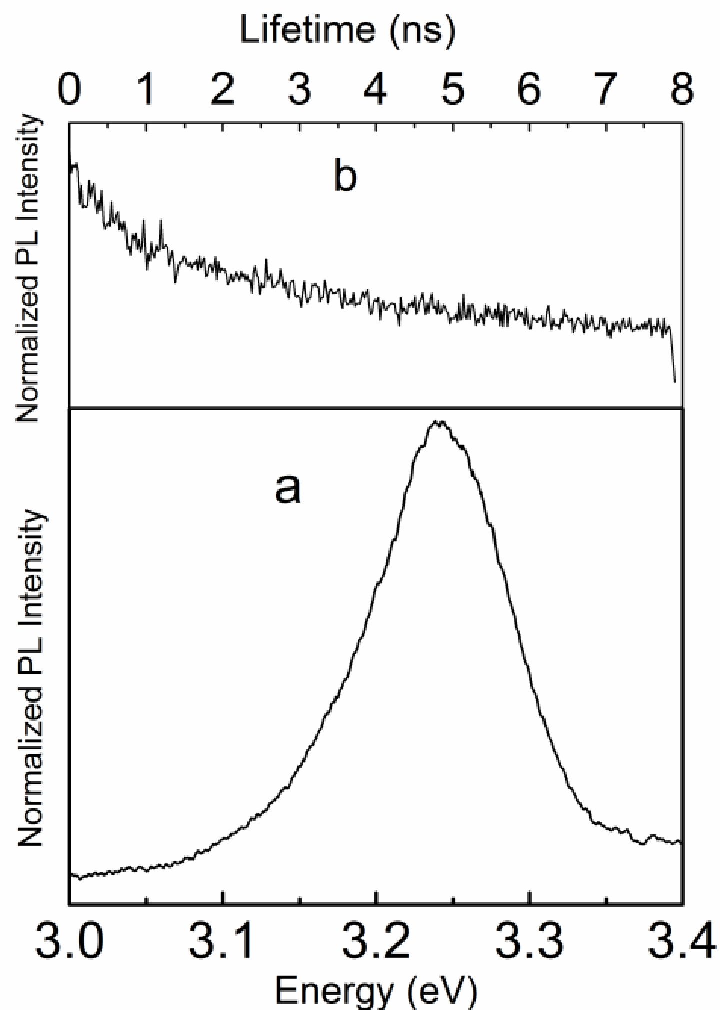

Figure 4.3 (a) CW- PL spectrum of UV region at RT with excitation at 325 nm. (b) PL lifetime at 3.25 eV with excitation at 350 nm.

Confined bound-exciton emission in the UV region can be enhanced at RT due to exciton plasmon coupling induced by the Ag induced localized surface plasmon polaritons (LSP) [18]. For an appropriate size of the Ag nanoparticles, the localized surface plasmons

can be coupled to the emission from the Si nanoclusters in the UV region. We have observed that the average size of silver nanoparticles is ~6.5 nm, which yields a surface plasmon energy of ~ 3.27 eV as estimated from the theoretical Mie scattering. The average distance between Si nanoparticles and silver nanoparticles was observed to be about 20 nm from the TEM measurements. The silver nanoparticles have a relatively sharp resonance and are most favorable for the surface plasmon induced enhancement of the PL emission. The recombination lifetime of the electron-hole pairs, as estimated from the TRPL measurements, changes from ~ 2 ns to 400 ps in the presence of silver ion induced surface plasmon polaritons as shown in Fig. 4.3(b). If the carriers recombination at 15 K is considered to be dominated solely by radiative recombination process, the internal quantum efficiency (IQE) from the crystalline nanostructures is estimated to be 5% at RT.

Figure 4.4(a) shows the PL emission from Si NCs which emits in the blue region. The emissions observed at ~ 2.98, 2.84, and 2.63 eV emanates from Si-related defect center. The mechanism of emission for peaks centered nearly at 2.98 and 2.84 eV is possibly from excess Si defect centers in the Si nanostructures [22, 23]. Fourier transform infra-red (FTIR) spectroscopy measurement of the sample shows Si-O-Si vibration band ~1100 cm^{-1}, indicating the excess Si defects states[17]. It is likely to involve states produced by the Si-O–Si bonds at the surface of NCs or the interface between the Si NCs and the SiO_2 [23]. Figure 4.4(b) shows carrier decay life time which is similar to the relaxation from oxygen-related states. These states are evidently shallow as the decay life time and the carrier life time in these states is short in the range of 1-2 ns. The shorter life time is due to trapped bound exciton at the defect centers. The IQE in this case at RT is found to be 7% which is also significant for RT emission.

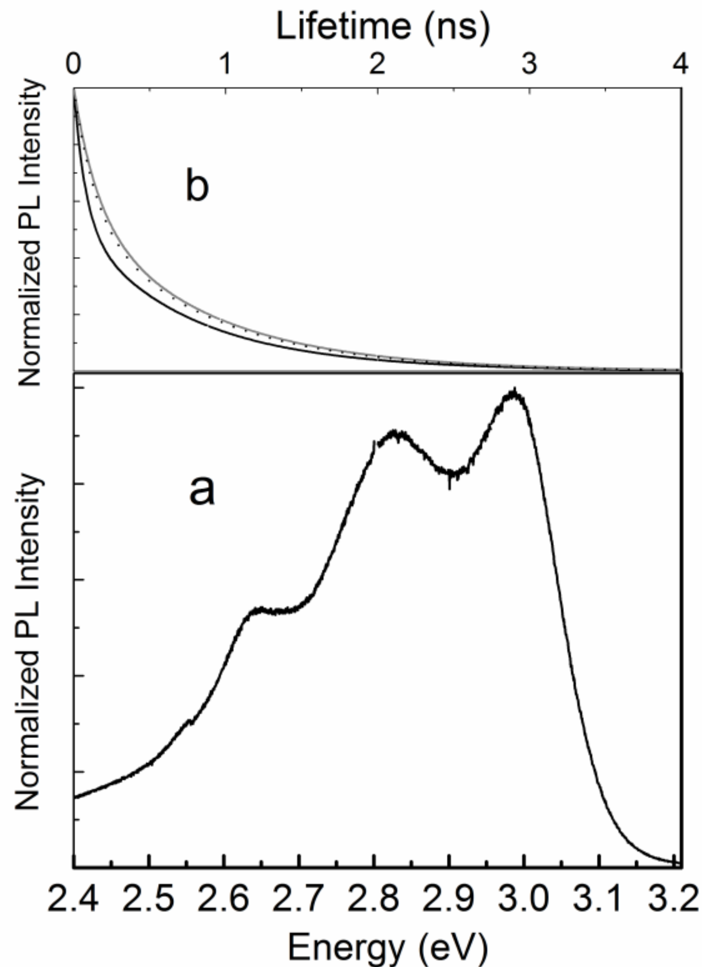

Figure 4.4 (a) CW- PL spectra of blue region at RT with excitation at 325 nm. (b) PL life time measured at 2.98 (solid), 2.84 (grey), and 2.63 eV (dashed) at 370 nm excitation.

Figure 4.5(a) shows the PL emission from Si NCs at 2.4 eV which is in the green region at RT. The green emission is only observed after annealing in an oxygen rich environment and wasn't observed in the case of the as-implanted samples. The green emission doesn't change significantly when annealed under inert gases, such as Nitrogen or Argon. It is observed that the emission efficiency at the green wavelength regime is significantly higher compared to the UV or blue emission and is estimated to be ~11% IQE at 300 K. The ns PL lifetime shown in fig. 4.5(b) indicates that the green PL peak emission arises from surface trapped excitons (STEs). The STEs are caused by the hole and electron localization at the surface of the NCs as reported by Pan et al. [24]. The ns PL decay time

compared to ms or μs lifetime eliminates the possibility of emission from quasi direct emission from the quantum confined states [25]. Thus, we can clearly conclude the origin of green emission on the basis of life time that emission is from STEs. There is no significant change in the PL lifetime due to the presence of the Ag nanoparticles which rules out the probability of surface plasmon mediated radiative recombination as observed in semiconductor light emitters. [29]

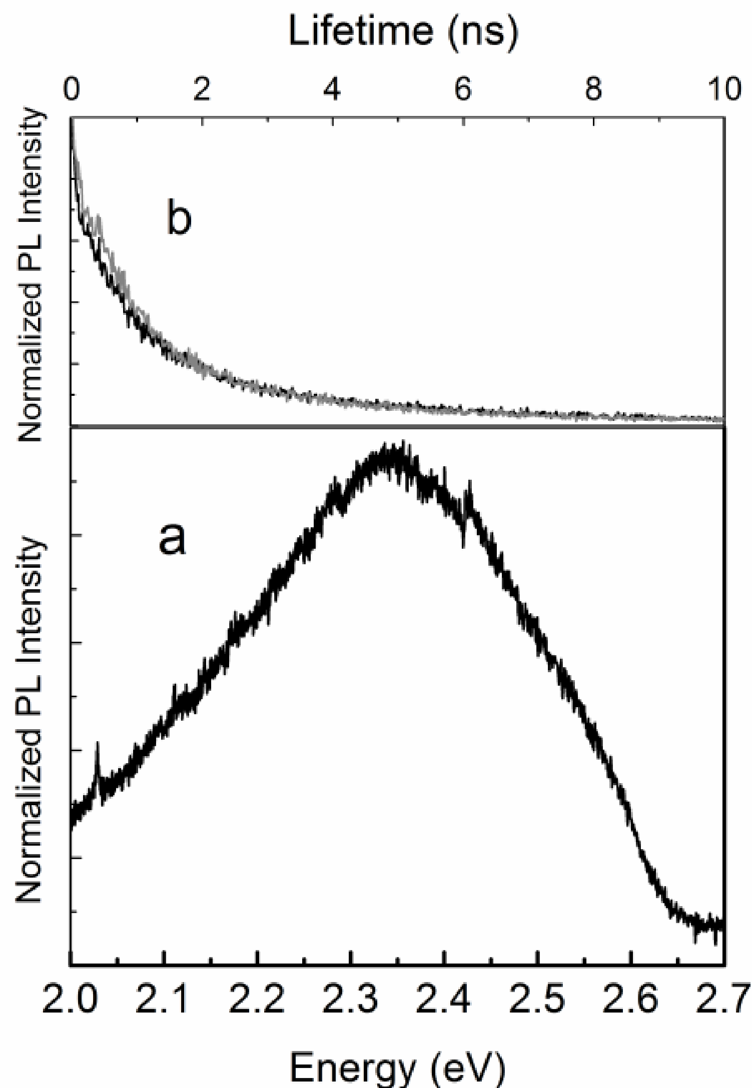

Figure 4.5 (a) CW- PL spectrum of the green region with excitation at either 325 or 442 nm. (b) PL lifetime measured at RT using ps excitation source at 400 nm.

Figure 4.6 shows the PL emission from Si NCs emitting in the NIR/red region. At RT, the PL peak is observed at 1.60 eV, which is likely due to the quasi-direct transitions in Si

NPs, and is caused by the partial confinement of holes and electrons. The effective mass theory can be applied to demonstrate that the origin of this emission is not from QC. The origin of the emission is attributed to defects in the SiO_2 matrix [28]. The PL lifetime could not be measured as the emission is rather long lived compared to the repetition rate of the pulsed laser. In addition, the emission intensity is rather weak under the influence of the fs pump compared to a CW excitation source. The IQE of the red emission is observed to less than 3% at RT.

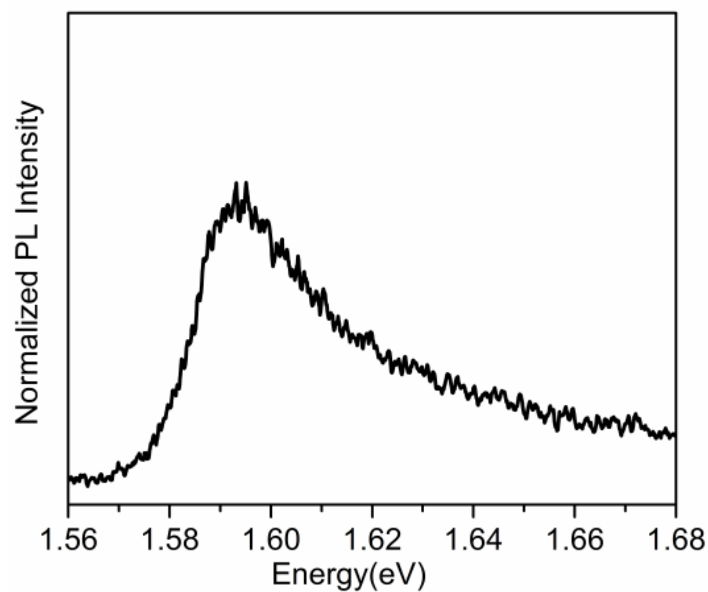

Figure 4.6 RT CW- PL emission in the near IR region with excitation at 442 nm.

Figure 4.7 shows the photoluminescence excitation (PLE) spectra in the UV and blue wavelength region, which depicts the absorption states associated with the light emission in the UV and blue regimes [17]. The PLE spectra in the UV region was measured with detector at 3.3 eV, whereas for the visible wavelength region, it was measured with the detector at energies 2.98, 2.84 and 2.63 eV. It has been observed that the presence of the high energy states at 4.14 eV is likely to influence the emission at 3.27 eV. In case of PLE in the blue wavelength regime, another high energy state at 3.28 eV also exists along with 4.14 eV as shown in Fig. 4.4 and confirmed in Fig. 4.7. The emission peak at 3.28 eV is independent of

the detection energy. It is also observed that the PLE properties in the blue wavelength remain unchanged for the various emission energy states. It can be clearly seen from Fig. 4.7 that the UV emission at ~ 3.27 eV has its origin from the absorption energy states exceeding 4.45 eV. Thus, as observed in [28], we can conclude from the PLE spectra of the UV and the blue region that the PL energy is not a characteristic of the emission from the quantum confined structure and supports the fact that the origin of emission is from localized defect bound-excitons.

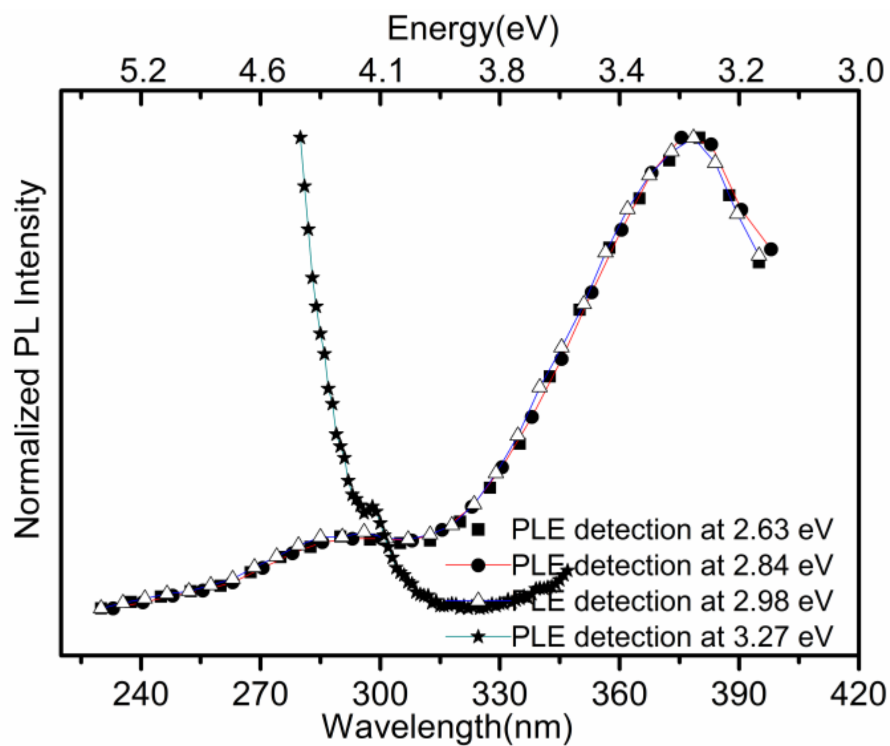

Figure 4.7 PLE spectra measured with the detector in the UV and Blue emission energies to show the presence of electronic states for carrier transitions.

4.4 Conclusion

We studied the origin of broad band tunable light emission from the UV to the red in metal implanted into silicon on the basis of CW-PL measurements, which is further strengthened and confirmed by life time measurements. The emissions at various wavelengths ranging from the UV, blue, green and red wavelengths were observed on the

same silicon substrate which was implanted with 32 keV Ag ions at a relatively shallow depth with a fluence of $5*10^{15}$ ions/cm^2. The formation of the nanocrystals increases the surface area at the interface of the crystalline Si and SiO_2 or amorphous Si layer. This results not only in an increased probability of forming surface trapped excitons resulting in the green emission, but also results in an exchange between the localized defects and Si nanocrystals formed due to annealing after the implantation process. It is observed that spectra in the UV and the blue region remains unchanged except for the enhancement of light in the case of post annealing compare to pre annealing. The IQE of the UV emission is enhanced due to the presence of the resonant localized plasmon modes generated at the surface of the Ag nanoparticles, which are nucleated due to annealing. The blue PL is also observed, whose origin is possibly from defects at Si/SiO_2 interface. CW- PL combined along with TRPL in the green emission region suggests that origin of emission is from STEs. The TRPL measurements also show that the localized plasmon modes do not affect the recombination of the STEs. A further detailed quantitative study will be helpful for controlling the STEs or QC emissions, which can fulfill the requirement for optoelectronic devices for integrated circuits and a new generation of flash memory.

4.5 References

1. L. T. Canham, Appl. Phys. Lett. **57**, 1046 (1990).
2. V. Lehmann, and U. Gosele, Appl. Phys. Lett.**58**, 856 (1991).
3. S. S. Iyer, and Y. H. Xie, Science **260**, 40 (1993).
4. S. Tiwari, F. Rana, H. Hanafi, A. Hartstein, E. F. Crabbé, and K. Chan, Appl. Phys. Lett. **68**, 1377 (1996).
5. R. M. Sankaran, D. Holunga, R. C. Flagan, and K. P. Giapis, Nano Lett. **5**, 537 (2005).
6. D. Zhang, R. M. Kolbas, P.D. Milewski, A. I. Kinngon, and J. M. Zavada, Appl. Phys. Lett. **65**, 2684 (1998).

7. A. Arbouet, M. Carrada, F. Demangeot, V. Paillard, G. BenAssayag, C. Bonafos, A. Claverie, S. Schamm, C. Dumas, J. Grisolia, M.A.F. Van den Boogaart, J. Brugger, L. Doeswijk, J. Lumin. **121**, 340 (2006).

8. L.J. Mitchell, O.W. Holland, A. Neogi, J. Li. and F.D. McDaniel, J. Non-Crystalline Solids **352**, 2408 (2006).

9. L.-S. Liao, X.-M. Bao, N.-S. Li, X.-Q. Zheng, N.-B. Min., J. Lumin. **68**,199 (1996).

10. B. Averboukh, R. Huber, K. W. Cheah, Y. R. Shen, G. G. Qin, Z. C. Ma, and W. H. Zong, J. Appl. Phys. **92**, 3564 (2002).

11. G. Hadjisavvas and P. C. Kelires , Phys. Rev. Lett. **93**, 226104 (2004).

12. C. Delerue, G. Allan, and M. Lannoo Phys. Rev. B **48**, 11024 (1993).

13. B. Delley and E. F. Steigmeier, Phys. Rev. B **47**, 1397 (1993).

14. S. Öğüt, J. R. Chelikowsky, Phys. Rev. Lett. **79**, 1770 (1997).

15. AL L Efros, A L Efros, Sov. Phys. Semicond. **16**, 772 (1982).

16. A.K. Singh, K.G. Gryczynski, S. Y. Park, M. Kim and A. Neogi, **151**, 1405 (2011).

17. A.K. Singh, K.G. Gryczynski, F. D. McDaniel, S. Y. Park, M. Kim and A. Neogi, Appl. Phys. Express **3**, 102201 (2010).

18. N.-M. Park, C.-J. Choi, T.-Y. Seong, and S.J. Park, Phys. Rev. Lett. **86**, 1355 (2001).

19. X. Yang, X. L. Wu, S. H. Li, H. Li, T. Qiu, Y. M. Yang, P. K. Chu, and G. G. Siu, Appl. Phys. Lett. **86**, 201906 (2005).

20. S. Godefroo, M. Hayne, M. Jivanescu, A. Stesmans, M. Zacharias, O.I. Lebdev, G. van tendeloo and V.V. Moshchalkov Nature Nanotechnology **3**, 174 (2008).

21. X. L. Wu, S. J. Xiong[1], G. G. Siu, G. S. Huang, Y. F. Mei, Z. Y. Zhang, S. S. Deng, and C. Tan, Phys. Rev. Lett. **91**, 157402 (2003).

22. L. Tsybeskov, Ju. V. Vandyshev, and P. M. Fauchet, Phys. Rev. B **49**, 7821 (1994).

23. X.-W. Pan, M.-M Shi, D.-X Zheng, N.L. Liu, G. Wu, M. Wang, H.-Z. Chen, Materials Chem. and Phys., **117**, 517 (2009).

24. S.E. Douglas, E.P. Lindsay, Z. Yu, F.B. Paul, A.K. Brian, Nano Lett. **2**, 681 (2002).

25. P. R. Poudel, J. A. Paramo, P. P. Poudel, D. R. Diercks,Y. M. Strzhemechny, B. Rout, and F. D. McDaniel, Journal of Nanoscience and Nanotechnology, doi:10.1166/jnn.2011.5711(2011).

26. H. Chen , C. Li , Z. Jiao , Z. Yu , Z. Yang , Y. Jin , Z. Li , H. Song , Y. Gao , Y. Zhang , J. Zhu , M. Gong , X. Sun, Journal of Non-Crystalline Solids **354**, 4562 (2008).

27. K.S. Min, K.V. Scheglov, C. M. Yang, H. A. Atwater, M.L. Brongersna and A. Polman, Appl. Phys. Lett. **69**, 2033 (1996).

28. A. Neogi, H. Morkoç, T. Kuroda, and A. Tackeuchi, Opt. Lett. **30**, 93 (2005).

CHAPTER 5

LOCALIZED SURFACE PLASMON POLARITON ENHANCED RADIATIVE RECOMBINATION IN ION- IMPLANTED SILICON[‡x]

5.1 Introduction

Light emission from Si can be attained by synthesizing crystalline or amorphous Si in the nanoscale dimension embedded within higher bandgap materials such as SiO_2 or Si nitride matrix [1, 2]. Confinement of Si nanoparticles can also result in quantum -confined Si quantum dots that have relatively higher quantum efficiency compared to porous Si nanoparticle based emitters [3, 4]. The light emission from Si nanoparticles has been observed to arise from quasi-direct to indirect transitions as well as from defect- bound excitons [5, 6]. The resulting emission has been observed from the UV to the near-infrared wavelength range [2]. However, the radiative efficiency in these systems is rather low compared to conventional quantum -dot -based light emitters.

Ion beam techniques have recently been employed by various groups to generate a random distribution of Si nanoparticles within SiO_2, SiC or SiN system [7,8]. Ion implantation provides a route to synthesis of Si-based nanocrystals for VLSI compatible nanophotonic emitters. However, current approaches of the synthesis of Si nanoparticles use high-energy ion implantation in the MeV range, which can result in nonradiative defect centers in the crystal. Despite annealing processes, the surface reconstruction of the crystal lattice is inadequate and results in surface enhanced nonradiative recombination centers that are detrimental for light emission. In this current work, we utilize a low- energy ion beam (32 keV) for the nucleation of Si nanoparticles to reduce the surface and defect- induced non-radiative recombination process.

[‡x] This entire chapter is reproduced from [A. K. Singh, K. G. Gryczynski, F. D. McDaniel, S. Y. Park, M. Kim, and A. Neogi, "Localized surface plasmon polariton enhanced radiative recombination in ion-implanted silicon emitters," Appl. Phys. Express **3**,102201 (2010)], with permission from JJAP.

Si nanocrystals (NC) in the SiO_2 matrix normally exhibits quasi-direct inter-band transitions due to band mixing of direct and indirect gaps in a nanoscale environment. Compared to direct bandgap III-V or II-VI semiconductor nanoparticles, the radiative recombination coefficient of Si is rather low at room temperature (RT), $B \approx 1 \times 10^{-14}$ cm^3/s [9]. Therefore, even considering the defect- mediated recombination and Auger- assisted nonradiative transitions to be suppressed due to spatial localization of carriers in Si nanoparticles, the electron-hole recombination lifetime is observed to be in the range of ms to microsecond. Due to the quasi-direct nature of band-alignment in a Si/SiO_2 system, an improvement in the crystalline quality and reduction in the defect density are not sufficient to enhance the radiative recombination rate for efficient light emission process.

Recently, plasmonics has been proposed as a candidate for light enhancement in Si by Okamoto et al. [10]. Our group had demonstrated a tenfold enhancement in the radiative recombination rate of GaN- based dipole emitter by having a metal thin film (Ag) with surface plasmon polariton (SPP) energy resonant to the quantum well emission wavelength [11]. Resonantly coupled excitons or free carriers from the excited states decay via plasmon interaction, which results in a significantly shorter lifetime than the spontaneous emission or photoluminescence (PL) recombination lifetime of the system in the absence of the electromagnetic field due to the metal. This SPP exciton coupling process is a radiative decay engineering process, which can be influenced by the non-radiative recombination process due to Joule heating at RT. Thus, metal nanoparticles with localized surface plasmon modes are an alternative option to enhance the radiative recombination rate of a light emitter to increase the internal quantum efficiency of the system.

Metal- implanted Si light emitters are therefore an attractive option for increasing the relatively low radiative recombination process in Si light emitters. Ion beam techniques also have the advantage of utilizing various ion sources including semiconducting and metal ions

in tandem to synthesize Si nanoparticles with various dopant levels and tunable plasmonic properties. Recently, plasmon-enhanced infrared emission from optically doped MOS light sources has been demonstrated using Ag–SiO_2–Si structures [12]. In the current work, we demonstrate the enhancement of UV light emission due to resonant plasmonic interaction from Si nanoparticles. These Si nanoparticles are synthesized in crystalline Si using low-energy Ag ion implantation. The effect of localized surface plasmons polaritons on Si light emitters is studied by comparing this metal-semiconductor material system with Si ion-induced Si nanoparticles that have fundamentally similar light emission properties. A corresponding enhancement in the radiative recombination rate is also observed in these systems associated with the PL enhancement.

5.2 Results and Discussions

Figure 5.1 shows the localized surface plasmon resonance energy for an Ag-SiO_2 material system for metal particle size determined from electron microscopy. High resolution transmission electron microscopy (HRTEM) measurements show that the average diameters of the Ag nanoclusters are ~ 6.5 nm and are on an average around 20 nm (center to center distance) from the Si nanoparticles. From the Mie modeling theory [16], the localized surface plasmon (LSP) energy for silver particle diameters of ~ 6.5 nm is estimated to be about 3.2-3.4 eV. Figure 5.1 shows that any UV emission ranging from 364 - 384 nm can be resonantly coupled to the Ag nanoparticles formed by ion-beam implantation. This wavelength range is suitable for the emission from the quantum confined states of ~ 2 nm Si nanoparticles [4] or the interface states between the Si and its oxide namely the –SiO_3 group, which bonds to Si structural surface and results in a strong 370-nm photoluminescence [17]. To investigate the effect of the resonant SPP process on the Si light emission process, the PL emission wavelength of the particles around 370-380 nm was considered. The defect level emission

due to Si-O-Si or Si-SiO_2 bonds around 450-485 nm is off-resonant to the LSP energy and is not studied.

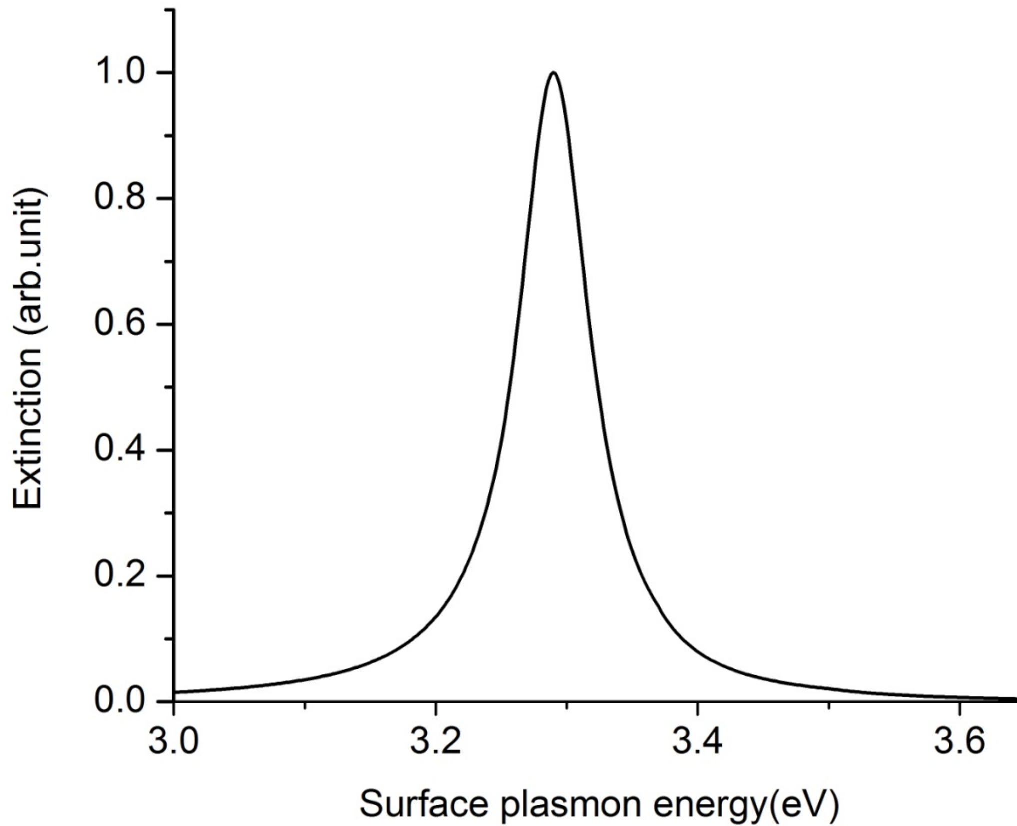

Figure 5.1 Localized surface plasmon resonance energy calculated from silver nanoparticles of average size 6.5 nm. The peak surface plasmon resonance energy in this graph is ~3.3 eV.

The Si nanoparticles are formed by implantation of ion using a low -energy ion beam, and the UV emission does not appear to be influenced by the nature of the ion beam. The Si nanoparticles were fabricated at RT using commercial ion beam implantation of Si(100) wafers using Ag and Si as the ion source. The detail of the synthesis process has been described elsewhere [13]. Similar sized nanoparticles are formed by Si, Ag or Au nanoparticles. The native oxide, which exists on the top of the Si crystal and is likely to form a thin oxide layer around the Si nanoparticles resulting a higher confinements necessary for light emission from a direct bandgap or quasi-direct bandgap emission in the UV wavelength.

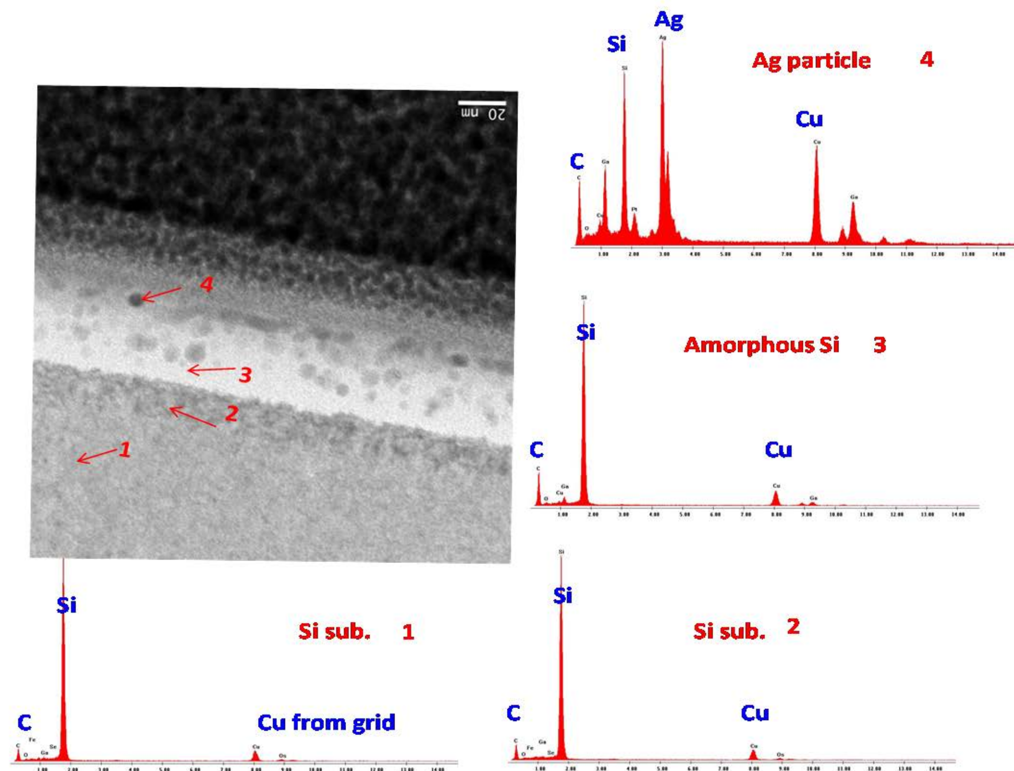

Figure 5.2 High resolution transmission electron microscope with EDX plots showing the presence of Ag nanoparticles in the proximity of Si nanoparticles. The Si nanoparticles are formed by the low energy Ag ion-implantation whereas the nanoscale Ag clusters are formed after annealing the samples at 5000 C. The carbon and copper signal in the EDX plots arise from the sample mount and TEM grid respectively

Crystalline Si nanoparticles have been synthesized in an amorphous Si matrix using implantation of keV Ag ions. For studying the effect of surface plasmon polariton on the exciton dissociation, we compare the emission from nanoparticles synthesized by Si ion induced implantation. HRTEM in Fig. (5.2) shows formation of Si nanoparticles, which emit at 3.3 eV at room temperature with a linewidth of 40-60 meV. The Stopping and Range of Ions in Matter (SRIM) estimates shows that the nanoparticle nucleates around the maximum energy of the ions penetrating the Si (100) lattice. The samples were annealed at 500^0C for an hour for the nucleation of Ag nanoclusters in the sample. The Ag nanoclusters are not observed before the annealing of the samples. An Energy –dispersive X-ray spectroscopy

(EDX) analysis shows that the Ag clusters in the proximity of the Si nanoparticles and is likely to result in a SPP coupling with excitons.

Figure 5.3 shows the PL emission from Si nanoparticles in the UV region measured using a HeCd laser source of excitation wavelength 325 nm. The emission from Si ion-implantation induced Si nanoparticles has a PL emission only at low temperature (below 160 K). RT emission cannot be obtained from as-implanted Si samples (with Si ion implantation). The peak PL intensities reduces by over 6 times as the temperature is varied from 15 K to 130 K. The narrow emission spectrum shows finer structures at low temperature due to contribution from the confined excitons as well as the interface states of the nanoparticles (see Fig. 5.3).

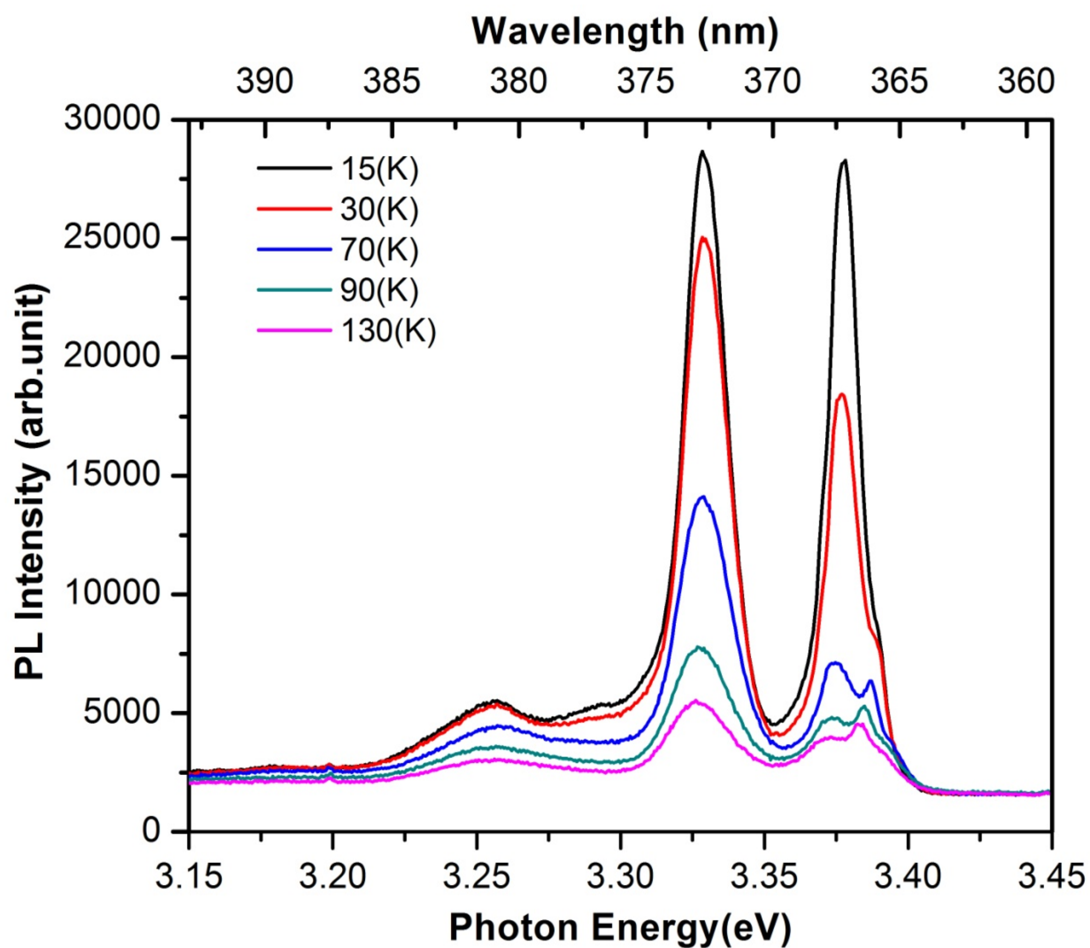

Figure 5.3 Temperature dependent PL from Si implanted Si nanocrystals observed using a CW excitation at 325 nm. PL emission is not observed beyond 160 K.

The recombinations of carriers in Si nanoparticles are mediated by the transverse optical phonon due to the polarization of the surface of the nanoparticles. The low- energy side of the emission spectrum at low temperature is dominated by 1st and 2nd - order phonon replicas showing the high quality of the nanoparticles. However, interface roughness at the Si/SiO_2 layer results in stronger nonradiative recombination which results in lower PL emission. One may assume that all of the carriers radiatively recombine at the lowest temperature (in our case 15K) and internal quantum efficiency (IQE) at say 160 K is derived by integral intensity ratio $I_{160\ K}/I_{15K}\times 100\%$. The internal quantum efficiency for Si implanted Si at 160 K is estimated to be 10%.

Figure 5.4 shows the temperature dependent PL emission which also exhibits PL emission beyond 160 K ; RT emission is also observed. The linewidth of the zero-phonon line emission at 374 nm is observed to be less than 50 meV, and is the narrowest linewidth reported in the case of Si based nanoparticles including Si quantum dots. Emission from the Si emitters in the ultraviolet region can be enhanced and RT emission can be observed due to exciton-plasmon coupling induced by the Ag- induced localized surface plasmon polaritons at the surface of the nanoparticles. The internal quantum efficiency of the Ag implanted Si system at 160 K is observed to be ~ 16% and at 300 K it is ~5%. However, a comparison of IQE can be misleading in the present case unlike in case of quantum well emitters due to the non-uniformity of the nanoparticle distribution in the presence and absence of Ag particles. The radiative recombination rate at low temperature and the Purcell enhancement is a better estimate as it is a fundamental property of an emitter and is not influenced by the absorption cross section.

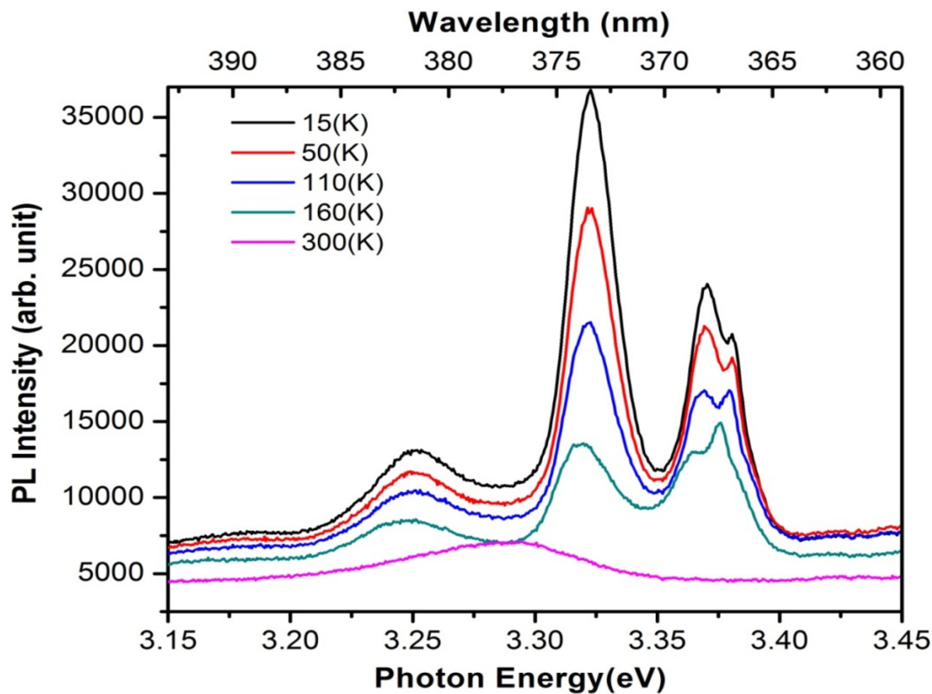

Figure 5.4 Temperature dependent PL from silver implanted Si nanocrystals observed using a CW excitation at 325 nm. UV PL emission is observed at 300 K in the presence of the Ag nanocrystals.

Figure 5.5 shows a comparison of the radiative recombination rate or the PL recombination lifetime measured using a Ti: Sapphire 80 MHz, femtosecond laser oscillator with a pulse width of 60 fs. The excitation wavelength doubled to 350 nm with an average power of 100 mW and the sample temperature was maintained at 15 K. It is observed from Fig. (5.4) that the PL recombination lifetime for the zero phonon line emission at 3.31 eV is significantly shorter than conventional Si based nanoparticles [14,15]. Bulk Si is an indirect bandgap semiconductor which does not exhibit light emission due to lack of radiative electron-hole pairs. In Si nanoparticles, the recombination lifetimes are typically in the ms to micro-second range. Additionally, the defects present in Si act as an efficient quencher for the emission process. However, as the Si particle size gets down to the nanoscale, the probability of carriers finding structural defects becomes very small and quantum confinement relaxes the selection rule, which promotes the radiative recombination process and prevents nonradiative recombination process. The probability of finding the structural defects in our

study is suppressed, which reduces the probability of nonradiative recombination processes and increases the probability of radiative recombination process. This is one of the main reasons that the life time gets shorter in the nanosecond range as reported in the case of blue emission [18, 19, 20]. Nanosecond PL decay times can be further enhanced to the picosecond domain due to localized surface- plasmon (LSP) -exciton coupling.

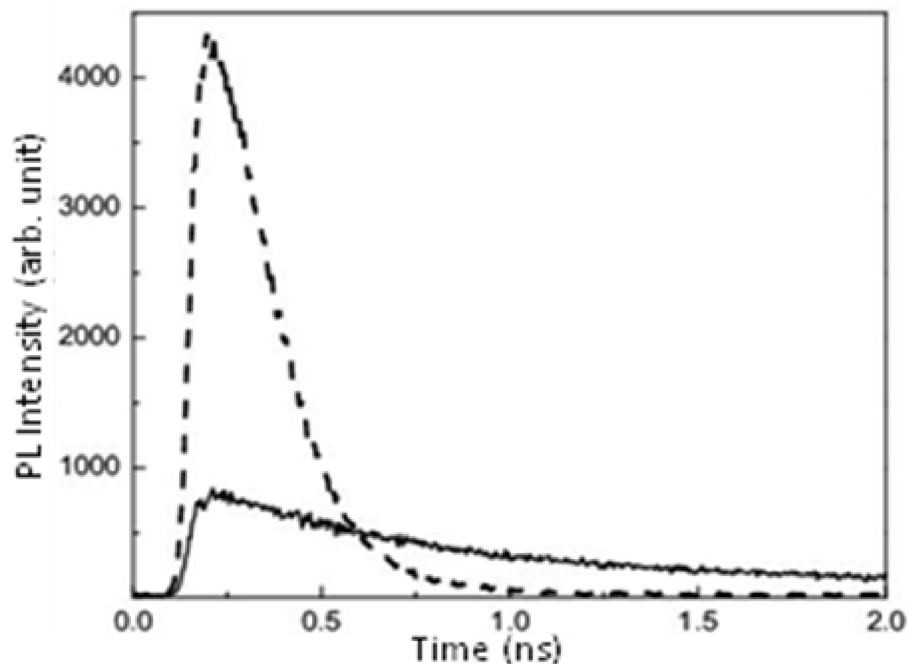

Figure 5.5 shows comparison of time-resolved photoluminescence emission from Si nanoparticles (at 15 K) in the presence of Ag at 3.31 eV. The dotted line represents the PL recombination rate from Si nanoparticle with (dashedline) and without (solid line) the Ag nanoclusters.

The Purcell enhancement factor, considered as the figure of merit for plasmonic light emitters has been plotted in Fig. 5.6. The Purcell factor is defined as the ratio of the radiative recombination lifetime of the Si nanoparticle without and with the Ag nanospheres. The Purcell factor is observed to be 4, which also agrees with the PL enhancement observed from the time-integrated PL spectrum shown in Fig.5.6. It is also observed that the high energy

emission at 3.37 eV is enhanced especially at 15 K.

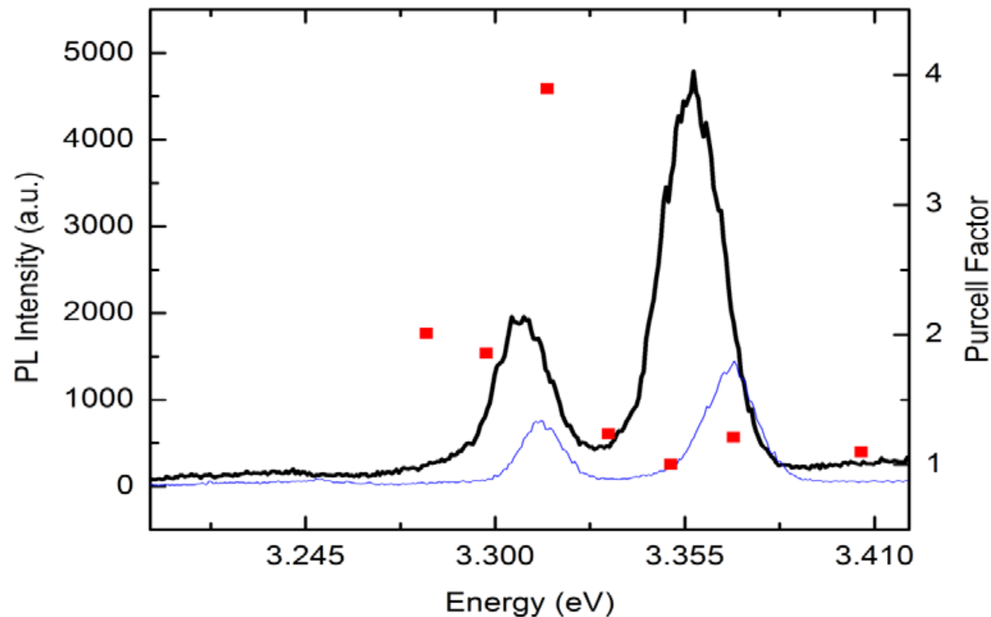

Figure 5.6 Time integrated PL measured at 15 K using femtosecond excitation source at 350 nm. The Purcell enhancement factor (τwo-Ag/τAg) is also shown on the other X-axis and corresponds to the four fold enhancement in the PL emission due to the pulsed laser excitation.

5.3 Conclusion

In conclusion, we have demonstrated a novel technique using low energy ion-beam implantation for generating localized surface- plasmon -enhanced emission from Si nanoparticles in the UV wavelength range. A large emission efficiency is observed at RT due to the presence of the Ag nanoparticles. The radiative recombination rate is enhanced by a factor of 5 at low temperature. However, the enhancement is significantly more at RT where no emission is observed without the Ag nanoparticle.

5.4 References

1. X. L. Wu, and F. S. Xue: Appl. Phys. Lett. **84,** 2808 (2004).
2. T. Kim, N. Park, K. Kim, G. Y. Sung, Y. Ok, T. Seong, and C. Choi: Appl.Phys. Lett. **85,** 5355 (2004).

3. I. Sychugov, R. Juhasz, J. Valenta, and J. Linnros: Phys. Rev. Lett. **94,** 087405 (2005).

4. N. M. Park, C. J. Choi, T. Y. Seong, and S. J. Park: Phys. Rev. Lett. **86,** 1355 (2001).

5. D. J. Lockwood, Z. H. Lu and J. M. Baribeau: Phy. Rev. Lett. **76,** 539 (1996).

6. K. Tomioka and S. Adachi: Appl. Phys. Lett. **87,** 251920 (2005).

7. A. Arbouet, M. Carrada, F. Demangeot, V. Paillard, G. BenAssayag, C. Bonafos, A. Claverie, S. Schamm, C. Dumas, J. Grisolia, M.A.F. Van den Boogaart, J. Brugger and L. Doeswijk: J. Lumin. **121,** 340 (2006).

8. L.J. Mitchell, O.W. Holland, A. Neogi, J. Li, and F.D. McDaniel: J. Non-Cryst. Solids **352,** 2408 (2006).

9. W. Gerlach, H. Schlangenotto and H. Maeder: Phys. Stataus Solidi A **13,** 277 (1972).

10. K. Okamoto, A. Scherer, and Y. Kawakami: Phys. Status Solidi C **5**2822**,** (2008).

11. A. Neogi, C-W. Lee, H. O. Everitt, T.Kuroda, A. Tackeuchi and Eli Yablonovitch: Phys. Rev. B **66,**153305 (2002).

12. A. C. Hryciw, Y. C. Jun, and M. L. Brongersma: Opt. Express **17,**185 (2008).

13. A. Singh, K. G. Gryczynski, B. Rout, J. Li, F. McDaniel, A. Neogi, G. Sahu, and D. P. Mahapatra: Fabrication, Particles, Characterization, MEMS, Electronics and Photonics Technical Proceedings of the 2009 NSTI Nanotechnology. Vol. **1**, 570 (2009).

14. I. Sychugov: Synthesis and properties of single luminescent Si quantum dots, Doctoral Thesis, Royal Institute of Technology, Stockholm, Sweden 2006.

15. A. Hryciw, A. Meldrum, K.S. Buchanan, C.W. White: Nucl. Instrum Method Phys. Res. B **222,** 469 (2004).

16. G. A. Shah: Kodaikanal Obs. Bull. Ser. A **2,** 42 (1977).

17. X. Yang, X. L. Wu, S. H. Li, H. Li, T. Qiu, Y. M. Yang, P. K. Chu, and G. G. Siu; Appl. Phys. Lett. **86,** 201906 (2005).

18. F. Huisken, G. Ledoux, O. Guillois, and C. Reynaud: Silicon Chemistry: From the Atom to Extended System, ed. P. Jutzi and U. Schubert (Weinheim, Wiley- VCH, p. 93(2003).

19. A. A. Bagabas, M. A. Gondal, M.A. Dastageer, A Al-Muhanna, T.H. Alanazi and M.A. Ababtain: Nanotechnology **20,** 355703 (2009).

20. L. Tsybeskov, Ju. V.Vandyshev, and P.M. Fauchet: Phys. Rev. B **49,** 7821 (1994).

CHAPTER 6

PHONON REPLICA AND NON PLASMONIC EFFECT IN SILICON NANOPARTICLES IN SILICON MATRIX

6.1 Introduction

This chapter begins with a brief discussion of different scattering processes and phonon replica observed in silicon systems. The splitting of PL in the UV region at low temperatures explains the mechanism of phonon replica, which is further strengthened by the Raman spectroscopy study.

6.2 Raman Effect

When a monochromatic radiation of very narrow frequency band is scattered by a substance then the scattered light not only consists of the radiation of incident frequency but also the radiations of frequencies above and below that of beam frequency. This form of scattering in which the frequency of the incident beam undergoes a definite change was observed and studied by Raman and is called the Raman effect.

The scattering process under consideration involves two photons overall, one incident and one scattered. Let E_i and E_f be initial and final energy state of the molecule, also let Ω_1, Ω_s and Ω_M be frequency of incident radiation, scattered radiation, and the difference between the initial and final states, respectively. For Raman scattering if E_f is greater than E_i then $\Omega_s = \Omega_1 - \Omega_M$ and we have stokes Raman scattering and; if E_f is less than E_i, then $\Omega_s = \Omega_1 + \Omega_M$ we have anti-stokes Raman scattering.

The Raman effect comprises a very small fraction, about 1 in 10^7. The anti-stokes line is much less intense than the stokes lines. This occurs because only molecules that are vibrationally excited prior to irradiation can give rise to the anti-stokes line. Hence, in Raman

spectroscopy, only the more intense stokes lines are normally measured. A simplified energy diagram which illustrates the Raman effect is shown below.

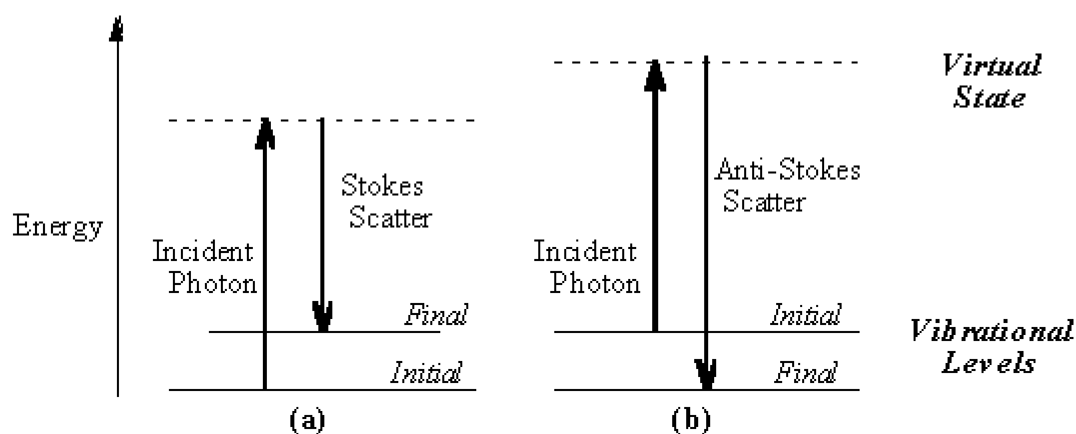

Figure 6.1 Energy level diagram for Raman scattering; (a) Stokes Raman scattering (b) anti-Stokes Raman scattering.

6.2.1 Classical Theory of Raman Effect

If an atom or molecule is placed in an electric field, the electrons and nuclei are displaced; electrons are attracted to the positive pole whereas nuclei to the negative pole. An induced dipole moment is produced in the molecule due to the displacement of the positive nuclei and the negative electrons, and the molecule is said to be polarized. If F is the strength of the electric field and μ is the magnitude of induced dipole moment, then

$$\mu = \alpha F \tag{1}$$

where α is the polarizability of the molecule.

The strength, F of the electric field of an electromagnetic wave of frequency υ, can be expressed as

$$F = F_0 \sin 2\pi\upsilon t \tag{2}$$

where F_0 is the equilibrium value of the field strength.

From equation (1), we have

$$\mu = \alpha F_0 \sin 2\pi\upsilon t$$

implying that the interaction of frequency υ induces in the atom or molecule a dipole moment which oscillates with the same frequency υ. By classical theory, this oscillating dipole should scatter radiation of the identical frequency υ, i.e. when the incident and scattered frequencies will be equal is a case of Rayleigh scattering.

If the molecule is diatomic, then as the two nuclei vibrate along the line joining them, the polarizability of the molecule will vary. The variation in polarizability α with small displacement x from equilibrium position is given by

$$\alpha = \alpha_0 + \frac{\beta x}{A} \tag{4}$$

where α_0 is equilibrium polarizability, β is the rate of vibration of the polarizability displacement and A is vibrational amplitude.

Without going into mathematical detail, we see that vibrational Raman shift is equal to the frequency of vibrational of the diatomic molecule.

Quantum Theory of the Raman Effect:

From a quantum viewpoint, we know that the vibrational energy levels are quantized. These levels can be properly described in terms of the number of quanta of excitation in each of the normal modes. In fact, each of these normal modes acts like a harmonic oscillator with energy in the nth state given by

$$E_n = \hbar\Omega(n + \frac{1}{2})$$

where n quanta of excitation are involved, Ω is the classical angular frequency of the particular oscillator.

In scattering, due to the absorption of the incident radiation by the scattering molecules, they are raised to a higher energy state. Now, if they return to their original state, then frequency of radiation emitted is same as that of incident light: but if they return to a

higher or lower vibrational or rotational level, the frequency of scattered radiation is less or greater than that of the incident radiation -the amount of this difference is equivalent to the difference in vibrational or rotational energy states. Let us consider a molecule in its initial (lower) state E_i and the molecule is exposed to incident radiation of frequency Ω_1. The absorption of this incident radiation would raise this molecule to its energy is ($E_i + \hbar\,\Omega_1$). Now suppose it returns to a level of energy E_f lying above the level E_i, losing energy $\hbar\,\Omega_s$ and emitting (scattered) radiation having observed frequency Ω_s. It follows then

$$E_i + \hbar\,\Omega_1 - \hbar\,\Omega_s = E_f$$

$$\text{Or, } E_f - E_i = \hbar\,(\Omega_1 - \Omega_s)$$

$$= \hbar\, c\, \Delta\upsilon \qquad (5)$$

where $\Delta\upsilon = \dfrac{\Omega_1 - \Omega_s}{c}$

This shows that the Raman shift $\Delta\upsilon$ is equal to the difference in energy of the two levels represented by E_f and E_i.

6.2.2 Raman Spectroscopy (Experimental)

Raman spectrum of Si as-implanted and annealed samples was measured using a Raman spectrometer T 6400 Horriba Jobin Yvon. Raman measurements were performed using laser excitation with an Ar ion green laser source of wavelength 514 nm. Charge coupled device (CCD) array of detector was used to collect Raman spectra, which provides information about the vibrational properties of materials.

Red and black line in fig. 6.2 shows Raman spectra of Ag implanted into silicon and Si unimplanted, respectively. It can be seen clearly that Raman shift for Ag implanted Si and Si unimpanted Si are at 512 and 521 cm^{-1}respectively. The TO phonon replica seen at lower temperatures in fig 6.2 can be correlated with the Raman shift. This Raman shift in Si phase

is due to TO phonons confined with microcrystals with diameter of several hundred angstroms. It is well documented in the literature that the peak frequency decreases from the value of 520 cm^{-1} to 512 cm^{-1} for a crystalline size of nearly 35 Angstroms [2]. Thus, the TO phonon replica seen at lower temperatures, which is already explained in above section well agrees with the Raman shift.

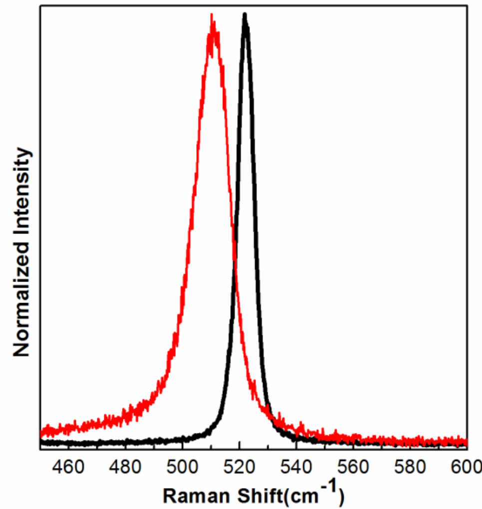

Figure 6.2 Raman spectra of Si unimplanted and Ag implanted in Si sample.

6.3 Non Plasmonic (Image Charge Effect)

The application of plasmonics in silicon based light emitters is of increasing interest due to the possibility of realizing Si based integrated photonic systems [3-10]. Ion implantation of Silicon or noble metal ions into Silicon, SiC, SiN, SiO2 or porous Silicon matrix can result in the formation of Silicon quantum dots or nanoparticles [1, 5-7, 8,11]. The spontaneous emission from the Si quantum dots or nanoparticles can be enhanced due to radiative recombination with plasmon channels that are within the electrodynamic coupling range of the metal nanopatterns or metal quantum dots with localized plasmon energy overlapping with the emission energy. Resonant coupling for the enhancement of the radiative recombination rate depends on the proximity or overlap of the surface-plasmon

energy at the metal-semiconductor interface to the emission energy of the quantum confined structure. For metal nanoparticles, the resonant coupling conditions are further restricted as the localized surface plasmon polariton mode is relatively narrow depending on its size distribution. Therefore, for enhancement of near-infrared light from Silicon nanoparticles, Au is the most preferred noble metal for resonant plasmonic coupling as the surface plasmon energy of thin films to nanoparticles ranges from the visible to the near-IR wavelength range (~ 2.0-1.55 eV). [3,5,8]. However, as quantum confinement of Si nanostructures and defect bound excitons emit light in the UV-visible wavelength regime, other metals with higher surface plasmon energy such as Ag and Al can be used for resonant surface plasmon coupling to the higher energy emission ranging from (4.0 -2.5 eV). The metal nano-patterns or metal nano-particles can be fabricated or self-assembled on the surface of silicon quantum dots or nanocrystallites for surface plasmon induced enhancement. In case of implantation of Si or metal ions in crystalline Si, an amorphous layer is formed at the surface, the depth of which depends on the energy on the implantation energy. The Si nanocrystallites of radius R are formed as a continuous medium of dielectric constant ε_{in} embedded in another medium of dielectric constant ε_{out}. The electrostatic potential is dominated by the surface polarization charge distribution given by the last term of the equation [1] for $\varepsilon_{in} >> \varepsilon_{out}$. [13]

$$V_c(r) = -e^2\left[\frac{1}{\varepsilon_{in} r} - \frac{1}{R}\left(\frac{1}{\varepsilon_{in}} - \frac{1}{\varepsilon_{out}}\right)\right] \tag{1}$$

The surface polarization charge also termed as the 'image-charge' results in an electrostatic attraction between the carriers and their images induced within the metal represents another mechanism for interaction. For a substantial difference between εin and εout, the Coulomb charging effects is significant as the induction of one extra electron in a previously neutral nanocrystallite will create an "image" surface charge distribution leading to a potential energy $e^2/\varepsilon_{out}R$ inside the cluster. This can result in a blue shift of

the level occupied by this carrier and increases with more carrier accumulation, which can then result in an appreciable blue shift in the emission energy [12]. Image charges due to dielectric mismatch has been predicted to result in an enhancement of the exciton binding energy and the oscillator strength in strongly confined Silicon quantum dots [15]. The internal efficiency of a light emitting device is given by

$$\eta = Bn^2/(An+Bn^2) \qquad (2)$$

where An is the nonradiative component and is dominated by Auger recombination processes in Silicon nanocrystals. In bulk silicon, the Auger process is very efficient and is proportional to $C(pn^2+np^2)$ where p, n are the hole and electron concentrations respectively and A,B are of the order of 10^{-31} cm^6s-1 [14]. The Auger recombination process in Si nanocrystallites is in the order of 0.1-1 ns and the lifetime decreases with increasing temperature [12]. Moreover, unlike direct bandgap III-V or II-VI semiconductor nanoparticles, the radiative recombination coefficient of Si is rather low at room temperature (RT), $B \approx 1 \times 10^{-14}$ cm^3/s [15]. Therefore, the light emission efficiency due to radiative recombination within Si nanocrystallites is rather low. However as the radiative component has a quadratic dependence on the carrier concentration n, $\Gamma_r = Bn^2$, a mechanism to enhance the carrier concentration in the recombination process can dominate the Auger mediated nonradiative recombination process and result in enhanced light emission from Si nanoparticles.

The presence of metallic nanoparticle induces a stronger image charge effect compared to image-charges due to the dielectric contrast. Image charges, being of equal magnitude and opposite sign to the image-inducing carrier, cause both electrons and holes to drift towards the surface of a nanoparticle located within the local field. Coulomb attraction of the carriers to the metallic nanoparticle (NP) increases the local concentration of electron-hole (e-h) pairs, leading to a strong enhancement of photoluminescence (PL). This

generalized electrostatic mechanism is not restricted by the frequency matching conditions imposed on SP coupling, and provides a means for enhancing non-resonantly the efficiency of solid-state emitters. Here, we report evidence of this effect in an ion-implanted silicon with gold nanoparticles and compare the effect with silver nanoparticles, which has resonant plasmonic coupling with the light emission from the higher energy Si NP emitter. The minimum size of the metal nanoparticles (NPs) exhibit the highest localized surface plasmon energy (LSP). Thereby considering an average particle size distribution of ~ 6.5 nm diameter for the Ag NPs ~ 2 nm for the Au NPs, the LSP energy has been calculated using Mie theory [18]. Figure 6.2 shows a comparison of the LSP energy due to the metal NP's with respect to the experimentally measured RT -PL energy of Silicon nanocrystallite (NC) emitter for the Ag and Au implanted samples.

It is observed (as shown in fig. 6.3) that in case of the Ag ions implanted sample, due to the higher LSP energy of the Ag in Si, there is a partial overlap of the emission energy to the surface plasmon energy.

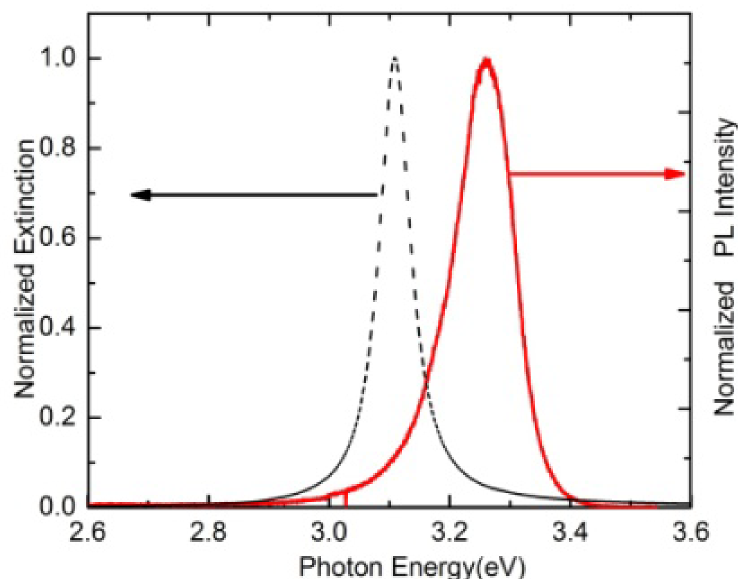

Figure 6.3 A comparison of normalized extinction coefficient (dotted lines) with respect to the room temperature PL emission energy from Si nanocrystals for Ag ion implanted sample.

The proximity of the Ag NPs close to the Si NCs facilitates resonant surface plasmon coupling. In figure 6.4, it can be observed that the LSP energy is significantly lower than the PL emission energy of the Si NCs formed due Au ion implantation. This energy mismatch eliminates any electrodynamic coupling of the UV photons to the low energy LSP modes. However, the presence of Au nanoparticles within the electrostatic coupling range can result in the image-charge effect influencing the PL. Room temperature PL is observed from the Au and Ag ion implanted sample which is not observed for the reference sample (created using Si ion implantation) having identical emission energy. The luminescence from Si NPs are normally observed in the NIR wavelength regime (~ 800 nm).

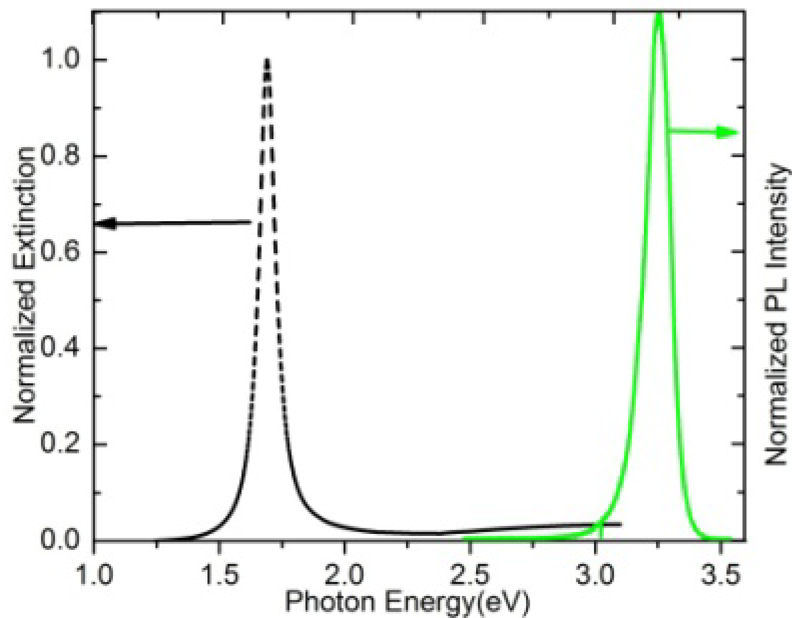

Figure 6.4 A comparison of normalized extinction coefficient (lines) with respect to the room temperature PL emission energy from Si nanocrystals for Au ion implanted sample.

However, the presence of an oxide layer due to annealing of the sample in atmospheric air or unintentional oxidation of the surface and presence of oxygen impurities can result in the formation of Si nanoparticles in SiO_2 matrix. [19] The emission in the UV wavelength region is due to the emission from defect bound excitons at the interface of crystalline Si NCs and

SiO_2 layer. Excitons, bound to the NPs with the metal nanoparticles, are sufficient for the manifestation of the electrostatic image charge effect. Emission from quantum confinement states within a NP is not essential for the generation of the image charge effect as the carriers (e-h) pairs form its image inside the metal surface and the dominant Coulomb attraction results in accumulation of carrier around the NCs. The LSP energy being detuned from the emission energy, the scattering or directional emission from the Au nanoparticles is not possible and is negligible in case of Ag nanoparticles.

6.4 References

1. Derek A Long, the Raman Effect (John Wiley & Sons Ltd, (2002).
2. Iqbal, Z and Veprek, s. , J. Phys. C: Solid State Phys. **15**, 377(1982).
3. J. S. Biteen, D. Pacifici, N. S. Lewis, H. A. Atwater, Nano Letters **5**, 1768 (2005).
4. M. Makarova, G. Yiyang, C. Szu-Lin, Y. Nishi, S. Yerci, L. Rui, L.D. Negro, J. Vuckovic, J. Select. Top. in Quant. Electron. **16**, 132 (2010).
5. J. S Biteen, L. A Sweatlock, H. Mertens, N. S Lewis, A. Polman, H. A Atwater, J. Phys. Chem. **111**, 13372 (2007).
6. A. Hryciw, Y. Chul Jun, and M. L. Brongersma, Opt. Express **17**, 185 (2009).
7. A. Singh, K. G. Gryczynski, F.D. McDaniel, S. Y. Park, M. Kim and A. Neogi, Appl. Phys. Express **3**, 102201 (2010).
8. K. Okamoto, A. Scherer, and Y. Kawakami, Phys. Stat. Sol. (c) **5**, 2822 (2008).
9. K. Quang Le and P. Bienstman, DOI 10.1007/s11468-010-9168-1, (2010).
10. L. Rogobete, F. Kaminski, M. Agio, and V. Sandoghdar, Opt. Lett. **32**, 1623 (2007).
11. A. Arbouet, M. Carrada, F. Demangeot, V. Paillard, G. BenAssayag, C. Bonafos, A. Claverie, 11. S. Schamm, C. Dumas, J. Grisolia, M.A.F. Van den Boogaart, J. Brugger and L. Doeswijk, J. Lumin. 121, **340** (2006).
12. L.J. Mitchell, O.W. Holland, A. Neogi, J. Li, and F.D. McDaniel, J. Non-Crystalline Solids, **352**, 2408 (2006).
13. M. Lannoo, C. Delerue, G. Allan and E. Martin, Mat. Res. Soc. Symp. Proc. **358**, 13 (1995).
14. M. Iwamatsu, Jap. J. Appl. Phys. **37**, 5620 (1998).

15. E. Yablonovitch and T. Gmitter, Appl. Phys. Lett. **49**, 587 (1986).

16. W. Gerlach, H. Schlangenotto and H. Maeder, Phys. Stat. Solidi A **13**, 277 (1972).

17. D.B.T Thoai, R. Zimmerman, M. Grundmann and D. Bimberg, Phys. Rev. B **42**, 5906 (1990).

18. G. A. Shah, Kodaikanal Obs. Bull. Ser. A **2**, 42 (1977).

19. A.K. Singh, K. Gryczynski, S.Y. Park, M. Kim, and A. Neogi, Solid State Communications **151**, 1405 (2011).

CHAPTER 7

SUMMARY AND CONCLUSIONS

We have observed broad-band tunable light emissions from the UV to the NIR in silver ion implanted silicon substrates. The behavior of PL emissions in UV region suggests the origin of the emissions is from highly localized defects at the Si/SiO_2 interface. Luminescence in the blue and green regions is also observed and the origin is also possibly from defects at the Si/SiO_2 interface. CW photoluminescence, combined with PLE and effective mass theory, suggests that the origin of broad band emission is from surface trapped excitons. Further detailed quantitative study of the synthesis process is necessary for the generation of nucleation centers for controllable surface trapped excitons or quantum confined emissions. The realization of efficient silicon based broadband emitters can fulfill the requirement of optoelectronic devices for integrated circuits.

Light emission from silicon was achieved through the formation of crystal defect sites and silicon oxides in a silicon matrix by ion implantation. The produced luminescence centers are stable and the wafer may be stored in atmosphere. The ability to produce multiple wavelength emission from a single wafer through the same process may be useful for producing inexpensive white light emitters. Further investigation into the formation process is necessary to control the location and distribution of emitting regions throughout the wafer. Post processing such as annealing and etching may be used to enhance the emission and will be investigated in the near future.

We have demonstrated a novel technique using low energy ion-beam implantation for generating localized surface- plasmon -enhanced emission from Si nanoparticles in the UV wavelength range. A large emission efficiency is observed at RT due to the presence of the Ag nanoparticles. The radiative recombination rate is enhanced by a factor of 4 at low

temperature. However, the enhancement is significantly more at RT where no emission is observed without the Ag nanoparticle.

We studied the origin of broad band tunable light emission from the UV to the red in metal implanted into silicon on the basis of CW-PL measurements, which is further strengthened and confirmed by life time measurements. The emissions at various wavelengths ranging from the UV, blue, green and red wavelengths were observed on the same silicon substrate which was implanted with 32 keV Ag ions at a relatively shallow depth with a fluence of $5*10^{15}$ ions/cm^2. The formation of the nanocrystals increases the surface area at the interface of the crystalline Si and SiO_2 or amorphous Si layer. This results not only in an increased probability of forming surface trapped excitons resulting in the green emission, but also results in an exchange between the localized defects and Si nanocrystals formed due to annealing after the implantation process. It is observed that spectra in the UV and the blue region remains unchanged except for the enhancement of light in the case of post annealing compare to pre annealing. The IQE of the UV emission is enhanced due to the presence of the resonant localized plasmon modes generated at the surface of the Ag nanoparticles, which are nucleated due to annealing. The blue PL is also observed, whose origin is possibly from defects at Si/SiO_2 interface. CW- PL combined along with TRPL in the green emission region suggests that origin of emission is from STEs. The TRPL measurements also show that the localized plasmon modes do not affect the recombination of the STEs. A further detailed quantitative study will be helpful for controlling the STEs or QC emissions, which can fulfill the requirement for optoelectronic devices for integrated circuits and a new generation of flash memory.

We investigated the physics of silicon nanostructure for technological applications. We observed broad band efficient light emission ranging from the UV to the NIR from a single Silicon wafer via plasmonic and non- plasmonic effects. In order to get the efficient

light emission from Si nanostructures, radiative decay engineering was very important. The splitting of the UV peak at lower temperatures was studied and finally conformed by PL and Raman spectra showing strong indication of phonon replica.